The Lermontov crater on Mercury: geology, morphology and spectral properties of the coexisting hollows and pyroclastic deposits

M. Pajola[1], A. Lucchetti[1], A. Semenzato[2], G. Poggiali[3,4], G. Munaretto[1,5], V. Galluzzi[6], G. A. Marzo[7], G. Cremonese[1], J.R. Brucato[3], P. Palumbo[8,6], M. Massironi[9].

[1]INAF-Astronomical Observatory of Padova, Vicolo dell'Osservatorio 5, 35122 Padova, Italy (maurizio.pajola@inaf.it); [2]Engineering Ingegneria Informatica S.p.A., Venezia, Italy; [3]INAF-Astrophysical Observatory of Arcetri, Firenze, Italy; [4]Università degli Studi di Firenze, Firenze, Italy; [5]Department of Physics and Astronomy "G. Galilei", Università di Padova, Padova, Italy; [6]INAF-Institute for Space Astrophysics and Planetology, Roma, Italy; [7]ENEA C. R. Casaccia, Roma, Italy; [8]DiST-Università degli Studi di Napoli "Parthenope", Napoli, Italy; [9]Geosciences Department, University of Padova, Padova, Italy.

Abstract

We present a multidisciplinary analysis of Lermontov crater, located at 15.24°N, -48.94°E in the Kuiper quadrangle of Mercury. By means of the MESSENGER multiband MDIS-WAC and monochrome MDIS-NAC images we prepare the first high-resolution geological map of the crater and its closest surroundings, highlighting the presence of coexisting hollows and pyroclastic deposits on its floor. Through the crater counting technique, we estimate a modelled age of the crater's floor ranging between 3.84 and 3.74 Ga. Since the thickness of the pyroclastic deposits located on the Lermontov floor is not quantitatively known, the derived modelled age can be either the one of the deposits themselves, or the impact age of Lermontov. In both cases, this age is older than the Mansurian one previously suggested for Lermontov, hence dating back the emplacement of the crater into the Late Tolstojan/Calorian timeframe. On the

photometrically corrected MDIS-WAC multiband dataset, we apply an unsupervised clustering technique that spectrally separates the different deposits located both inside and outside the Lermontov crater. We identify that the pyroclastic deposits located on the crater's floor have a steep, red spectral behaviour dominated by the presence of a mixture of various pyroxenes containing Ti, Ni and possibly Vanadium. On the contrary, the vents' rims are characterised by several hollows whose spectral slope is bluer than that of the pyroclastic deposits themselves. By comparing the vent hollows to the ones located farther out on the crater floor, we observe a 0.62-0.82 μm spectral trend that is more similar to the pyroclastic one. Their 0.55 μm absorption band could be related to CaS, while the small differences at 0.48 μm and 0.62 μm could be due to the presence of other volatiles compounds, such as MgS and Fe_3Cl. When compared to those located on completely different hermean geological settings, Lermontov hollows are characterised by steeper spectra. This supports the interpretation that such hollows formed entirely inside the pyroclastic material affecting their behaviour and are shallower than the pyroclastic thickness itself, hence postdating its formation.

Introduction

The Lermontov crater is a 166 km wide, 3.3 km deep crater located at 15.24°N, -48.94°E in the Kuiper quadrangle (-22° to +22°lat., 0° to -72°E long.) of Mercury (Fig. 1A). This crater was first identified in Mariner 10 images (DeHon et al., 1981) thanks to its particularly bright floor characterised by smooth plains (Fig. 1B). A first possible explanation for this brightness behaviour was given by Dzurisin (1977), which suggested that it might be the direct result of fumarolic alteration along multiple fractures located on the floor. Instead, Rava and Hapke (1987) noted how the crater floor appears to have a lower crater density than the surroundings. This aspect, coupled with the occurrence of irregular rimless pits in its northeast sector, was considered indicative of endogenic modification (Schultz, 1977). Rava and Hapke (1987) then

proposed that Lermontov bright interior might have been emplaced by pyroclastic activity, i.e. volcanic eruptions formed by the fragmentation and upward propulsion of magma particles driven by the expansion of volatile species released from rising bodies of magma (Wilson and Head, 1981).

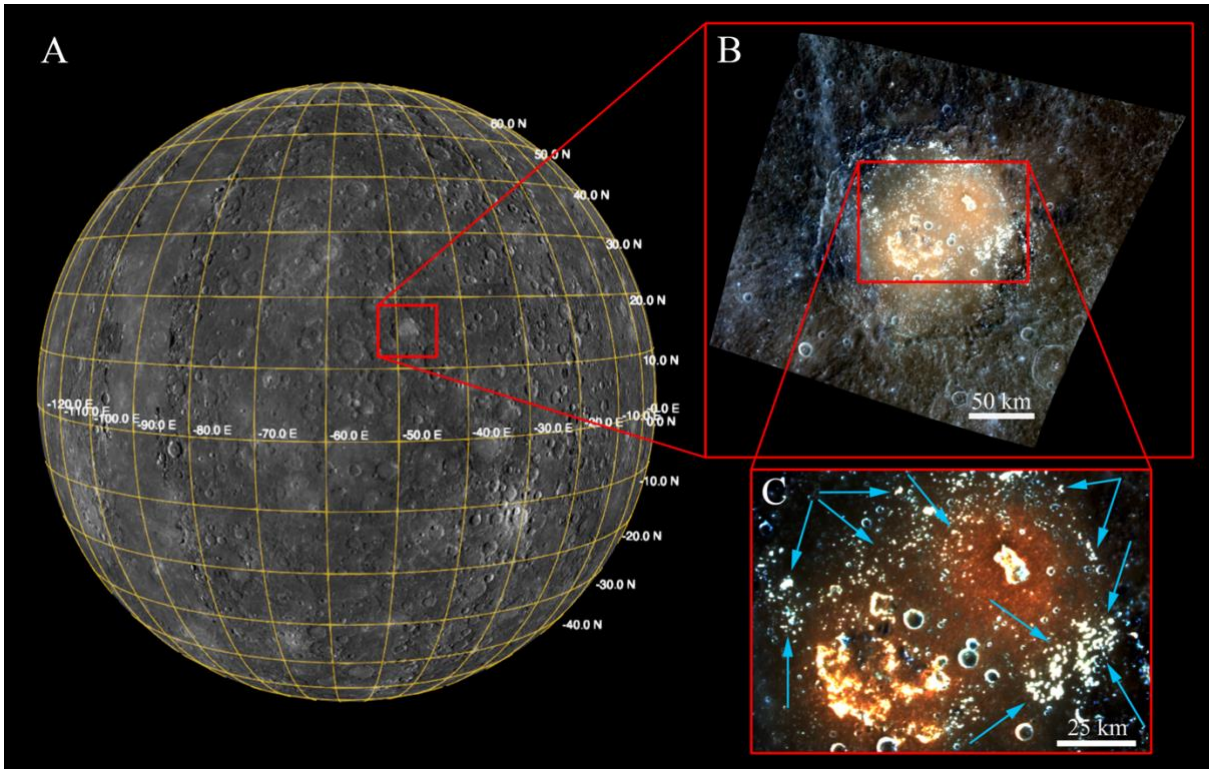

Figure 1. A) Context image of Mercury with the location of Lermontov crater (red square). B) MESSENGER MDIS-WAC RGB image of Lermontov (the red channel of the RGB is filter at 0.947 μm, the green channel is filter at 0.628 μm while for the blue channel we used the filter at 0.433 μm). C) Stretched RGB closeup showing the red pyroclastic deposits and the location (light blue arrows) of the hollows.

Using MESSENGER (Mercury Surface, Space, Environment, Geochemistry, and Ranging; Solomon et al., 2007) flybys 1-3 MDIS (Mercury Dual Imaging System, Hawkins et al., 2007) images, Kerber et al. (2011) eventually identified inside Lermontov floor two of the 35

pyroclastic deposits[1] elsewhere found on Mercury, together with their associated vents[2]: a smaller one located north-east that show crisp edges (Goudge et al., 2014), while a larger one with much more degraded edges situated south-west (Goudge et al., 2014). In particular, Kerber et al. (2011) suggested that the vent associated with the Lermontov NE pyroclastic deposit is morphologically similar to the one associated with the lunar pyroclastic deposit Sulpicius Gallus (Lucchitta and Schmitt, 1974; Gaddis et al., 2003), where a non-circular shape, rimless margins and lack of ejecta deposits is evident, but it is twice as large as the lunar one.

Pyroclastic deposits on Mercury generally appear to be brighter and redder, i.e. they show both higher reflectance than background terrain and a more steeply inclined visible to infrared reflectance slope (Robinson et al., 2008; Blewett et al., 2009, Kerber et al., 2009). This is the case for Lermontov deposits (Fig. 1C) that are classified in the Vis NIR range as "red" (Izenberg et al., 2014). The Lermontov crater floor is also of extreme interest because on its deposits there is a widespread distribution of hollows (Blewett et al., 2013), which are shallow, irregular and rimless flat-floored depressions with bright interiors and halos (Blewett et al., 2011; 2016), generally presenting a blue spectral trend (Vilas et al., 2016). Given both the pyroclastic and hollows' nature, their coexistence is of pivotal importance to provide information about Mercury surface, subsurface structure and composition (Wilson, 2009). Moreover, the presence of both pyroclastic deposits and hollows on Lermontov allows to compare both spectral trends, study their mutual mineralogies and uniquenesses, as well as it provides hints on the differences among such hollows with respect to those located on completely different hermean geological settings (Lucchetti et al., 2018).

[1] Pyroclastic deposits are identified through three lines of evidence (Kerber et al., 2009) using the Moon as the baseline for comparison: 1) diffuse boundaries, as those seen at the outer margins of deposits on Io known from observations to be fall deposits (Strom et al., 1981); 2) the near-circularity of the deposit, with its centre of symmetry that corresponds to the vent (this is consistent with the dispersal of ballistically transported pyroclasts from the vent itself); 3) the anomalous colour signature of the deposit in multispectral images, hence suggesting a layer of material with physical or chemical properties different from those of the pre-existing surface rocks.

[2] Irregular vents identified in over half of the identified deposits (Kerber et al., 2011) are distinguished from impact craters on the basis of their non-circular shape, rimless margins, lack of an ejecta deposit and lack of association with secondary crater chains.

The aim of this work is therefore to provide a detailed geological overview of the Lermontov crater together with its modelled surface age. Afterwards, we focus on the red pyroclastic deposits estimating both the possible volatile quantities that may have triggered the vent explosions, as well as their mineralogical composition. We then study the hollows spectrophotometric behaviour comparing their mineralogy with the pyroclastic deposits where they formed. Eventually, the differences of these hollows with those unrelated to pyroclastic activity are presented.

Material and Methods

Imagery and DTM for Geological Mapping

In order to prepare the geological map of Lermontov crater and its closest surroundings, we first imported the monochromatic MDIS Basemap Data Record[3] (spatial scale of ~166 m/pixel, Fig. 2A, see Supplementary Material Table 1 for all basemaps used) into the European Space Research Institute ArcGIS 10.5 software (hereafter ArcGIS).

To be able to map small features such as hollows located on the crater's floor (from tens to hundredths of meters in size), we also processed several MDIS NAC single frames into nine different mosaics using the U.S. Geological Survey (USGS) ISIS3 software (see Supplementary material Table 2). The resulting spatial scale of these mosaics range between 26 m and 48 m, covering a large part of Lermontov crater interior (Fig. 2B). For all images presented in this work, including full-crater views and close-ups, we adopted an Equidistant Cylindrical

[3] The MDIS BDR is a global map of I/F measured by the Narrow Angle Camera (NAC, Hawkins et al., 2007) or in the Wide Angle Camera (WAC, Hawkins et al., 2007) filter no. 7 (both centered at 0.749 μm) at moderate/high incidence angle, and then photometrically normalized to a solar incidence angle of 30°, an emission angle of 0°, and a phase angle of 30°, with a spatial sampling of 256 pixels per degree.

projection centred at 15.2°N; 48.9°E (with a sphere of 2439.4 km radius, Denevi et al., 2018), being also the projection used for geological mapping.

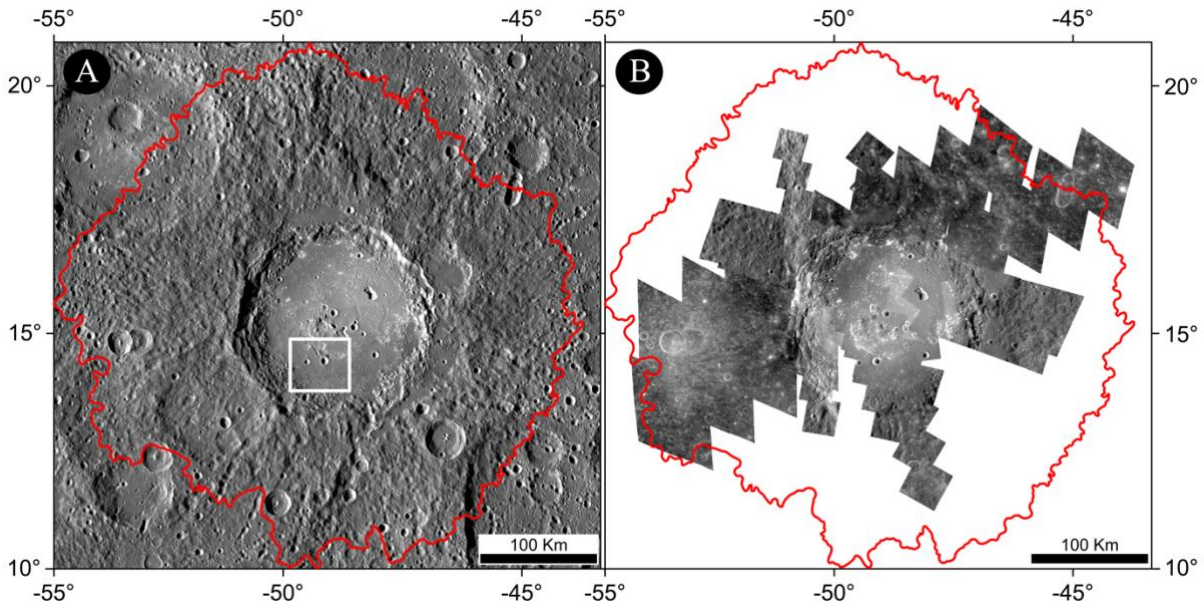

Figure 2. A) The MDIS BDR dataset (166 m/pixel) covering the Lermontov crater study area. The red line shows the extension of Lermontov ejecta. The white box shows the extension of Fig. 8A. B) The nine MDIS NAC mosaics (26 to 48 m/pixel) prepared for the high-resolution geological mapping.

We then downloaded the low-resolution MD3-color global mosaic (Fig. 3A), as well as the Enhanced-color basemap (both obtained from the MDIS and with a scale of ~665 m/pixel, Fig. 3B). On the two colour datasets, we applied the Image Sharpening Transformation technique (Color Normalized (Brovey) Sharpening, Thomas et al., 2014; Du et al., 2007; Parente and Pepe, 2017) obtaining the enhancement of their spatial resolution up to the level of the monochrome basemap, but maintaining the colour information (Fig. 3C, D). To complement this multiband dataset, we used the monochrome high-incidence angle and the low-incidence angle MDIS images (both with a scale of ~166 m/pixel, Fig. 4A, B) mapping the geological units by highlighting both “colours” and different textures, at an average scale of ~1:400.000.

We also took into account the USGS stereo-derived digital terrain model (DTM v2, with sampling of 665 m/pixel; Becker et al., 2016) of the area, which was used for a thorough interpretation of the surrounding surface morphology (Fig. 5).

Instead, thanks to the spatial scale provided by the NAC images available on Lermontov floor, all hollow-related features were mapped at a scale between 1:60.000 and 1:100.000. In the north-eastern part of the crater the hollows identification was aided by the 155 m scale DTM (Fig. 5) published by Fassett (2016). We followed the USGS digital cartographic standard for map symbolization (Fig. 6 and 7) in order to provide an exhaustive cartographic product (https://ngmdb.usgs.gov/fgdc_gds/geolsymstd.php).

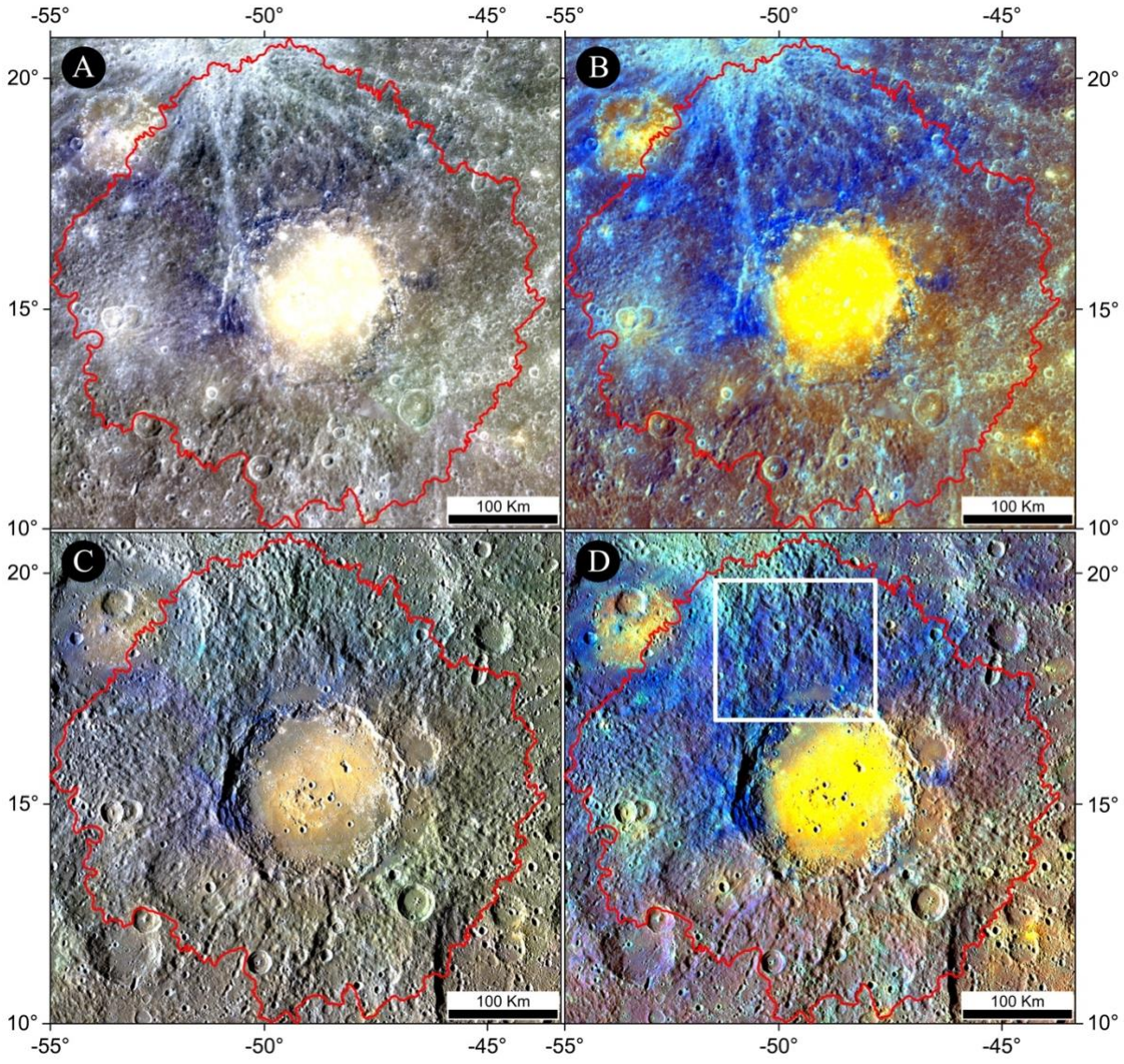

Figure 3. The Lermontov crater, whose ejecta extension is represented by the red line. A) MD3-color global mosaic (665 m/pixel), obtained by using the 0.996 μm, 0.749 μm and 0.433 μm narrow-band filters in the red, green and blue channels of the RGB, respectively. B) The MDIS Enhanced-colour basemap of Lermontov (665 m/pixel), obtained by using the second principal component, the first principal component, and the 0.433 μm/0.996 μm ratio in the red, green and blue channels, respectively. C) Color Normalized Brovey Sharpening of panel A (166 m/pixel). D) Color Normalized Brovey Sharpening of panel B (166 m/pixel). The white box shows the extension of Fig. 7A.

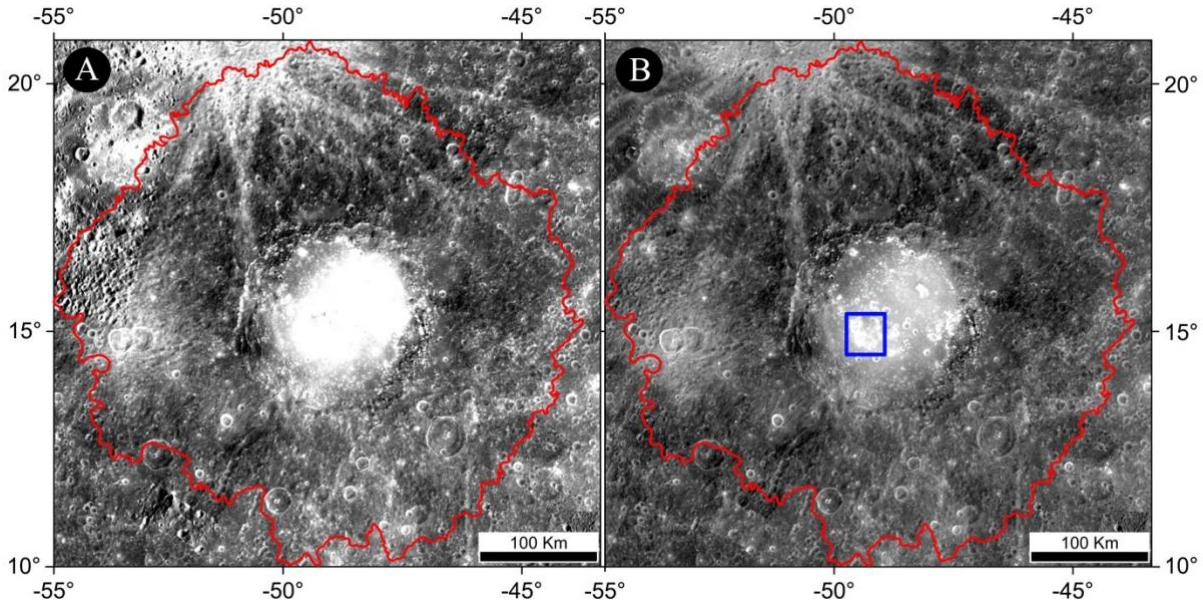

Figure 4. A) The MDIS high-incidence angle image (scale of ~665 m/pixel) covering the Lermontov crater study area. The red line shows the extension of Lermontov ejecta. B) The low-incidence angle image (scale of ~665 m/pixel). Both images are used to highlight the different textures of the geological units. The blue box shows the extension of Fig. 6A.

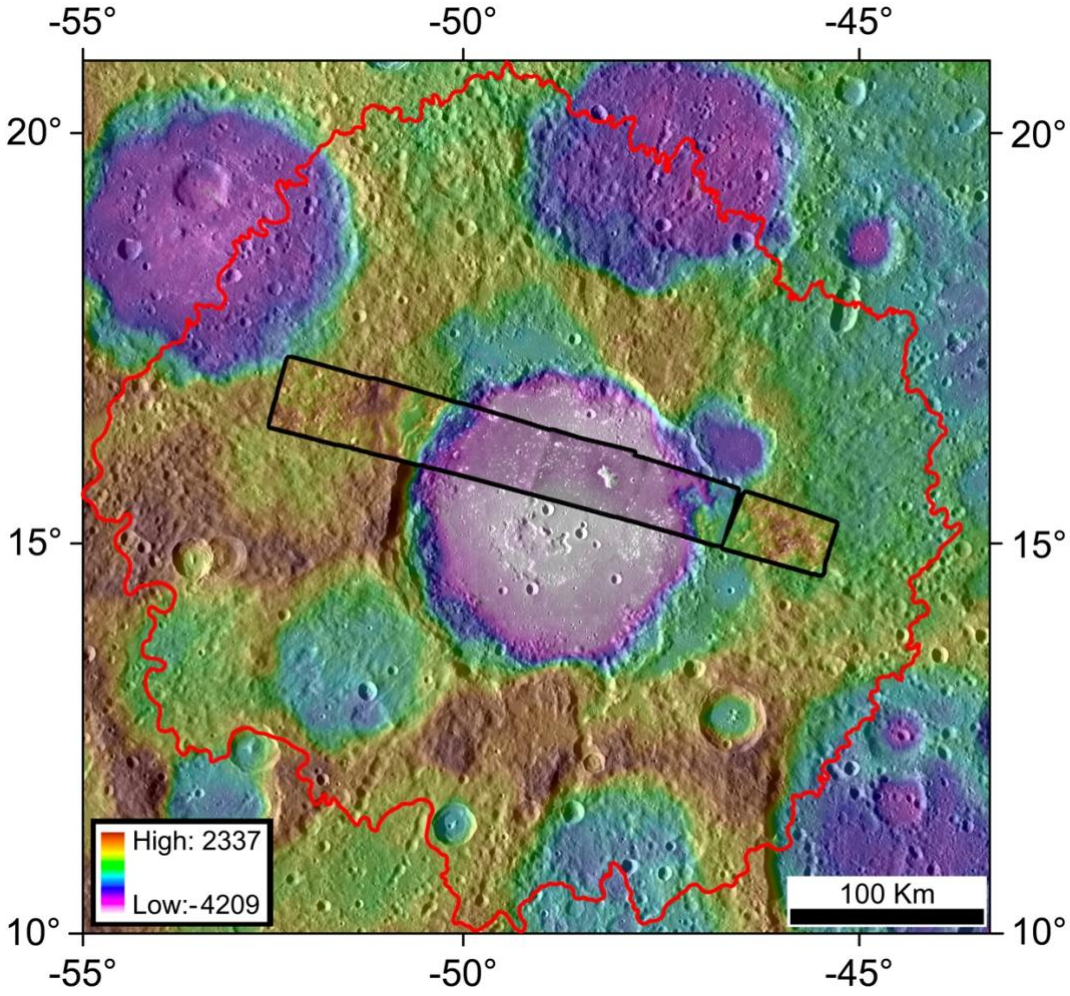

Figure 5. The USGS stereo-derived digital terrain model (spatial sampling of 665 m/pixel; Becker et al., 2016) covering the Lermontov study area. The red polygon shows the extension of Lermontov ejecta. The black rectangle shows the 155 m scale DTM prepared by Fassett (2016).

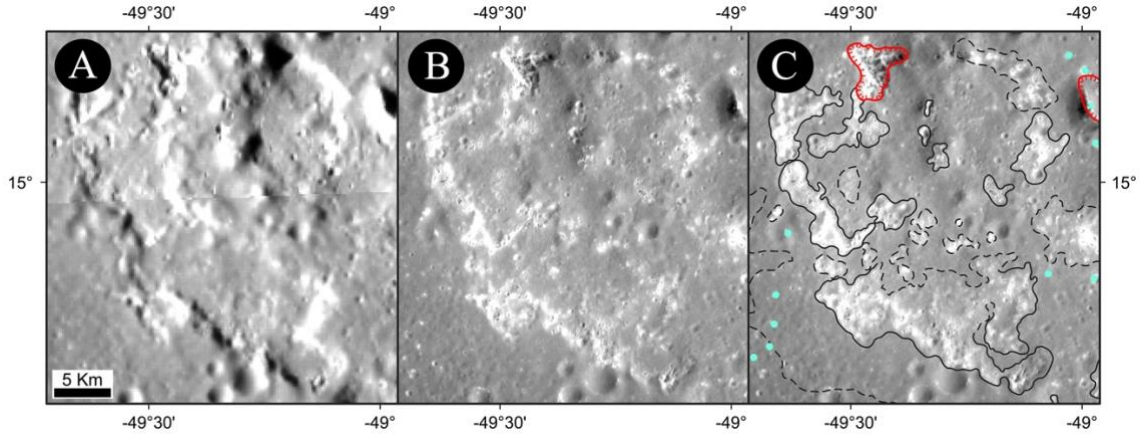

Figure 6. A) MDIS BDR close-up displaying hollow clusters and volcanic pits located in the south-west portion of Lermontov floor (the location is in Fig. 4B). B) High-resolution NAC Mosaic no. 1. C) Same as B) but with geologic contacts, linear and point features. The solid lines represent certain contacts, while dashed lines represent

approximate contacts; red lines with related ticks toward the inner slope scarp represent volcanic pit crests; light blue dots identify isolated hollows that are too small to be mapped as polygons (i.e. geologic units).

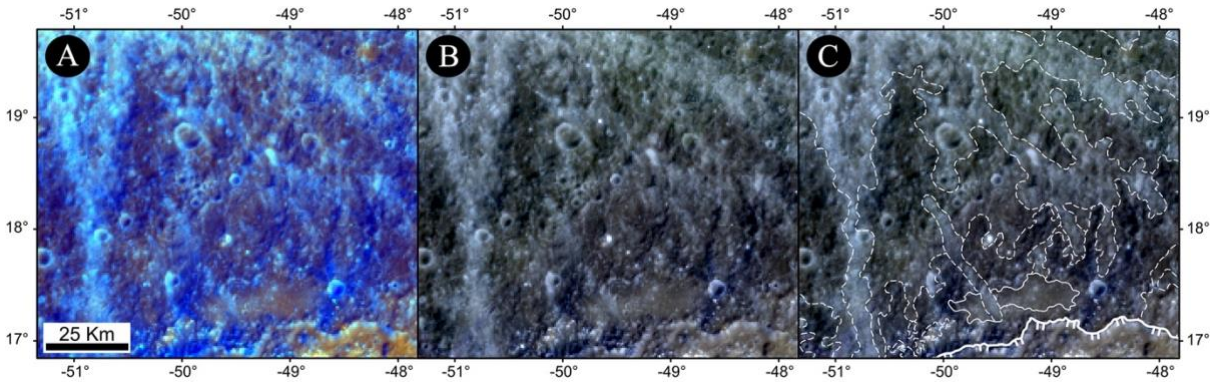

Figure 7. A) MDIS Enhanced-color global mosaic close-up situated North of Lermontov crater (the location is in Fig. 3D); B) MDIS MD3-color global mosaic; C) same as B) but with geologic contacts displaying the overlapping relations between Lermontov crater ejecta, Bark crater ejecta (with brighter colour), dark material and melt pool respectively excavated and produced by the Lermontov impact emplacement. Solid white lines represent certain contacts, while dashed white lines represent approximate contacts; the Lermontov crater rim is identified by a solid white line with ticks toward the inner wall scarp. For the geologic units associated to these contacts the reader is referred to the main geologic map (Fig. 11).

Crater Identification

By merging both the MDIS-NAC 26-48 m-scale imagery mosaics and the monochromatic MDIS Basemap Data Record (166 m/pixel sampling), we have fully covered the Lermontov crater floor. As usually done in planetary sciences (e.g. Galluzzi et al., 2016; Pajola et al., 2016a,b) we outlined all visible craters as circles, limiting their sizes to the visible rims (Fig. 8A, B). Through the ArcGIS software we then extracted the area value for each crater and derived the corresponding sizes in km.

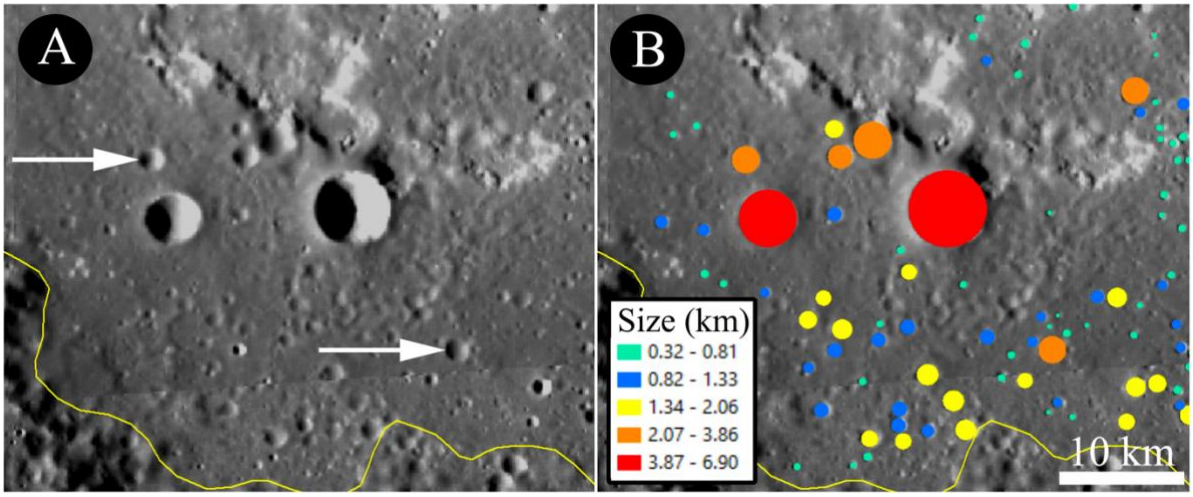

Figure 8. Methodology used to identify the craters located inside Lermontov floor (outlined with the yellow line). A) Subframe of the MDIS BDR dataset of Fig. 2A. The white arrows indicate the direction of the sunlight. B) The detected craters ≥0.3 km, grouped in size-categories (km).

Spectrophotometry and Clustering

To perform the spectrophotometric analysis of Lermontov deposits, hollows and their closest surroundings we used the MDIS-Wide Angle Camera (WAC, Hawkins et al., 2007) images. This multispectral dataset has a spatial scale of 266 m/pixel through 11 filter (0.433, 0.480, 0.559, 0.629, 0.699, 0.749, 0.828, 0.899, 0.947, 0.996 and 1.103 μm, see Supplementary Material Table 3). As done in Lucchetti et al. (2018), all images were photometrically corrected to the standard viewing geometry (i.e. incidence angle of 30°, emission angle of 0° and phase angle of 30°) using the Hapke model with parameters derived in Domingue et al. (2015). This was accomplished through the ISIS3 image processing package of the USGS (https://isis.astrogeology.usgs.gov/). Once the unnormalized photometrically corrected data set was obtained, we then focused on four different selections (Fig. 9), three with dimensions of 150 × 150 pixels, all located inside the crater's floor (Selection no.1, called Sel. 1, is located on the SW pyroclastic deposit, Sel. 2 is located on the NE pyroclastic deposit and vent, Sel. 3 lies on the hollow cluster situated in the central-east side of the floor), and one on the ejecta

deposits (100 × 100 pixels wide, called Sel. 4). On such MDIS multiband selections we then applied a statistical clustering based on a K-means algorithm developed and evaluated by Marzo et al. (2006). This algorithm makes use of the Calinski-Harabasz criterion (Calinski & Harabasz, 1974) to find the intrinsic number of clusters, making the process unsupervised. Each resulting cluster is characterised by its average spectrum and associated standard deviation. In addition, the relative geographical information of each spectrum is maintained in the process, and the resulting clusters can be located on the map. Therefore, correlations between spectral trends and geographical features can be investigated. This technique has been extensively validated using spectral data sets and applied to Mars (Marzo et al. 2006; 2008; 2009; Fonti and Marzo 2010), Iapetus (Pinilla-Alonso et al., 2011; Dalle Ore et al., 2012), Phobos (Pajola et al., 2018), Charon (Dalle Ore et al., 2018) and Mercury (Lucchetti et al., 2018). Since the Marzo et al. (2006) algorithm is agnostic of the physical and or mineralogical meaning of the resulting clusters a subsequent scientific interpretation is then required.

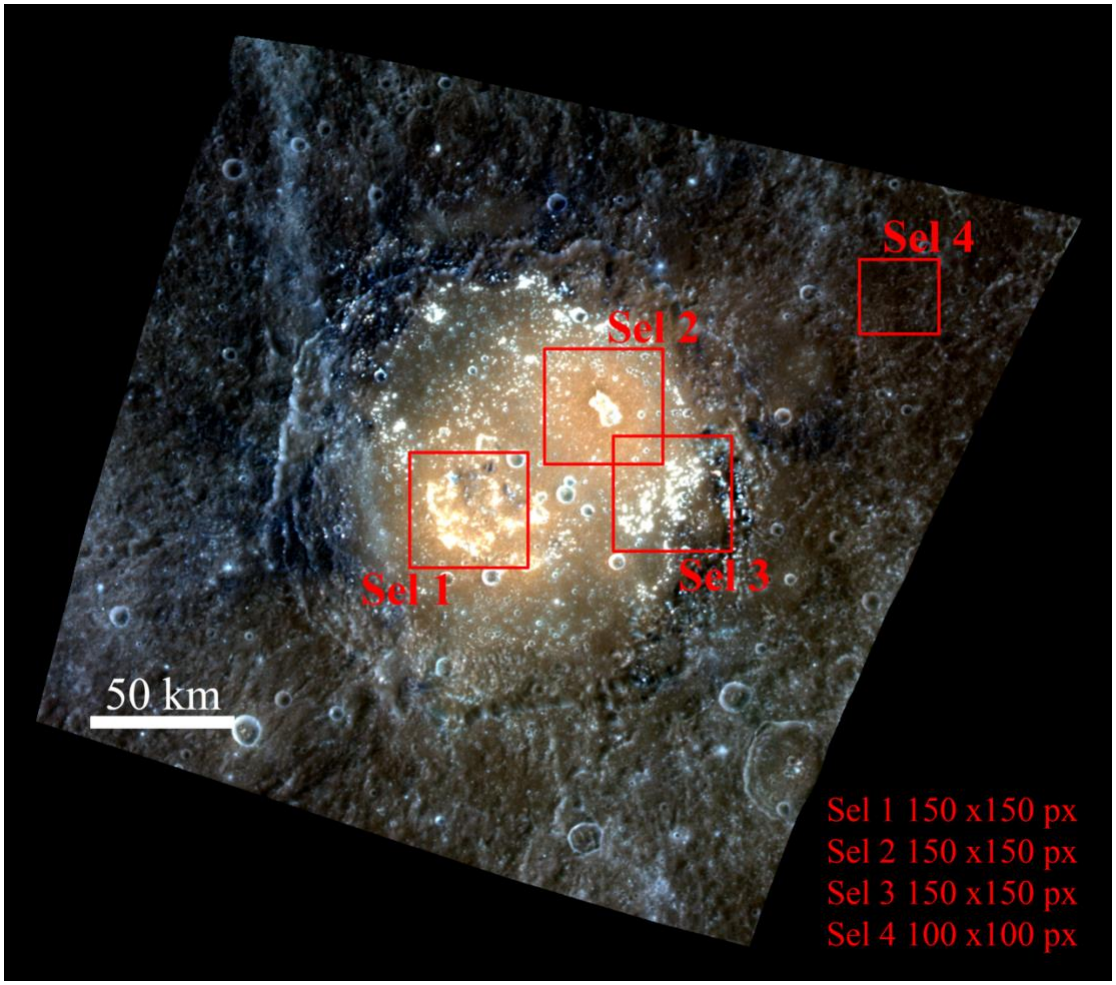

Figure 9. The four selected areas where we applied the spectral clustering technique. Three (Sel. 1, 2 and 3) are located inside Lermontov crater's floor, while one (Sel. 4), is located well outside the crater's rim inside the ejecta deposits.

Mineralogy

In order to identify the possible mineralogical composition of the different spectral clusters obtained, we performed a spectral matching with the data derived from the RELAB catalogue of the Brown University (http://www.planetary.brown.edu/relab/). This procedure allows the comparison between the RELAB spectra and the measurements performed through the 11 MDIS-WAC filters (taking into consideration wavelength, bandwidth and transmission for each of the 11 MDIS-WAC filters used, see Supplementary Material Table 3, Hawkins et al.,

2007). An example of the original spectrum, Ti-rich pyroxene PYX126 (RELAB id. PP-EAC-061/C1PP61), and the resampled one is showed in Fig. 10. Afterwards, the in-depth spectral analysis and comparison with laboratory spectra involved the continuum removing of clustered data in order to enhance the spectroscopic differences between each area under investigation.

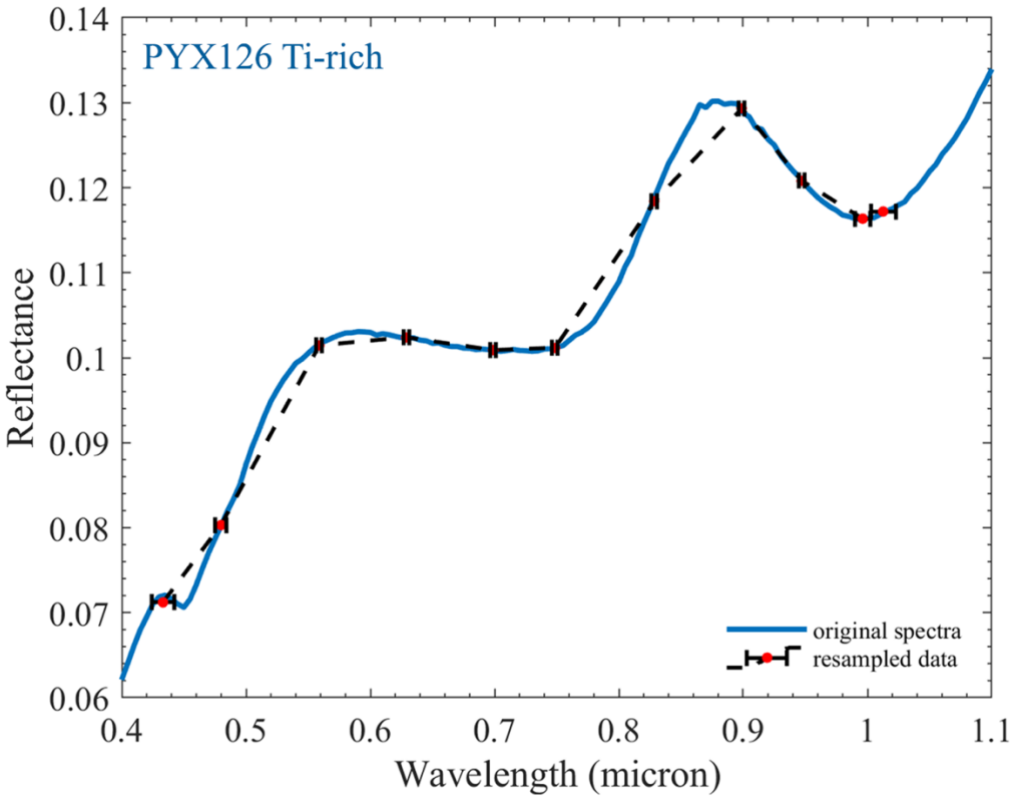

Figure 10. Ti-rich pyroxene from Cloutis (2002), solid blue line, and the resampling result (red circle and black dashed line). The horizontal bars represent the MDIS-WAC filter bandwidths.

Results

Geologic Map

Lermontov is a 166-km-sized crater, located at 15.24°N, -48.94°E. Its rim appears broadly degraded, with different levels of degradation: in fact, whereas in the western and northern parts it is identified by a sharp and still recognizable crest, in the south-eastern border it is strongly reworked by post-impact modification processes, which in some cases make its identification

difficult or not possible, suggesting a relatively old age of the crater. Consequently, the boundary of the ejecta deposits was hardly recognizable outside the Lermontov crater, and therefore, all the ejecta deposits were classified as a single unit, without distinguishing between proximal and distal ejecta (Fig. 11).

The slopes within the crater wall show a widely rough morphology, identified in the geologic map as ‘hummocky deposit’ and relatable to the wall talus (Fig. 12). Within the latter, multiple sets of terraces are visible, more developed in the western wall. These surfaces are usually delimited by steep scarps, whose margins were mapped when visible.

In particular, almost vertical scarps are found close to the rim border, characterised by extremely smooth deposit distinguished from the rough, hummocky deposit previously described, and originated from surface ‘polishing’ of mass wasting processes. These deposits were classified in the geologic map as ‘wall smooth talus’.

Furthermore, no evidence of central peak structures is found inside the crater. However, in the centre of the crater floor, there are some small domes and crests that could be interpreted as remnants of an old central peak, but they were nonetheless reworked and modified by irregular pits and vents, from which pyroclastic deposits (described below) likely erupted. In addition, some smooth areas outside the crater covering the ejecta deposits close to the rim, are identified as melt pools and interpreted as ‘impact melt’, related the impact event of the Lermontov crater.

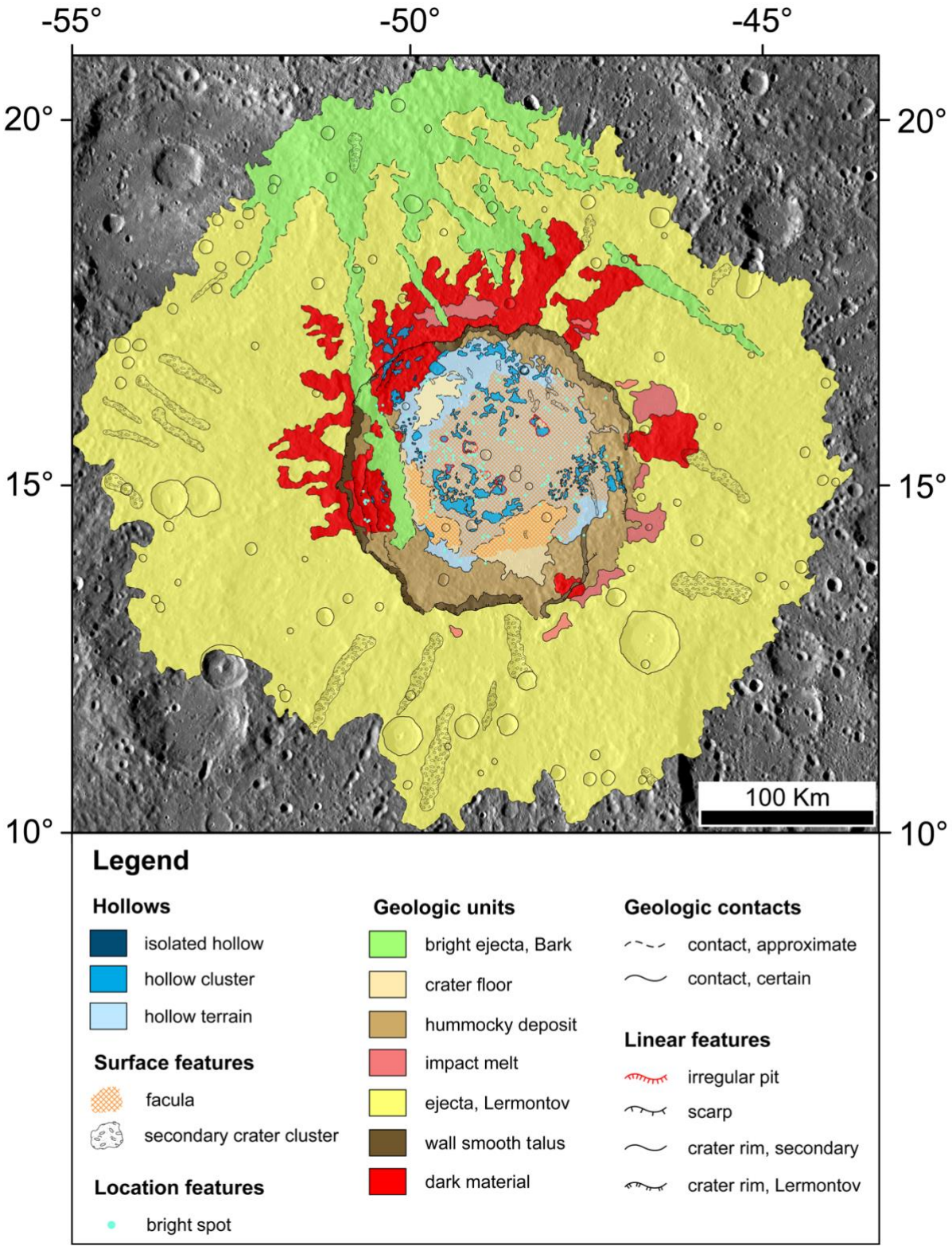

Figure 11. The Lermontov full geological map. The map projection is equidistant cylindrical with central meridian 311.1° and central parallel 15.2°. The planet radius considered is 2439.4 km.

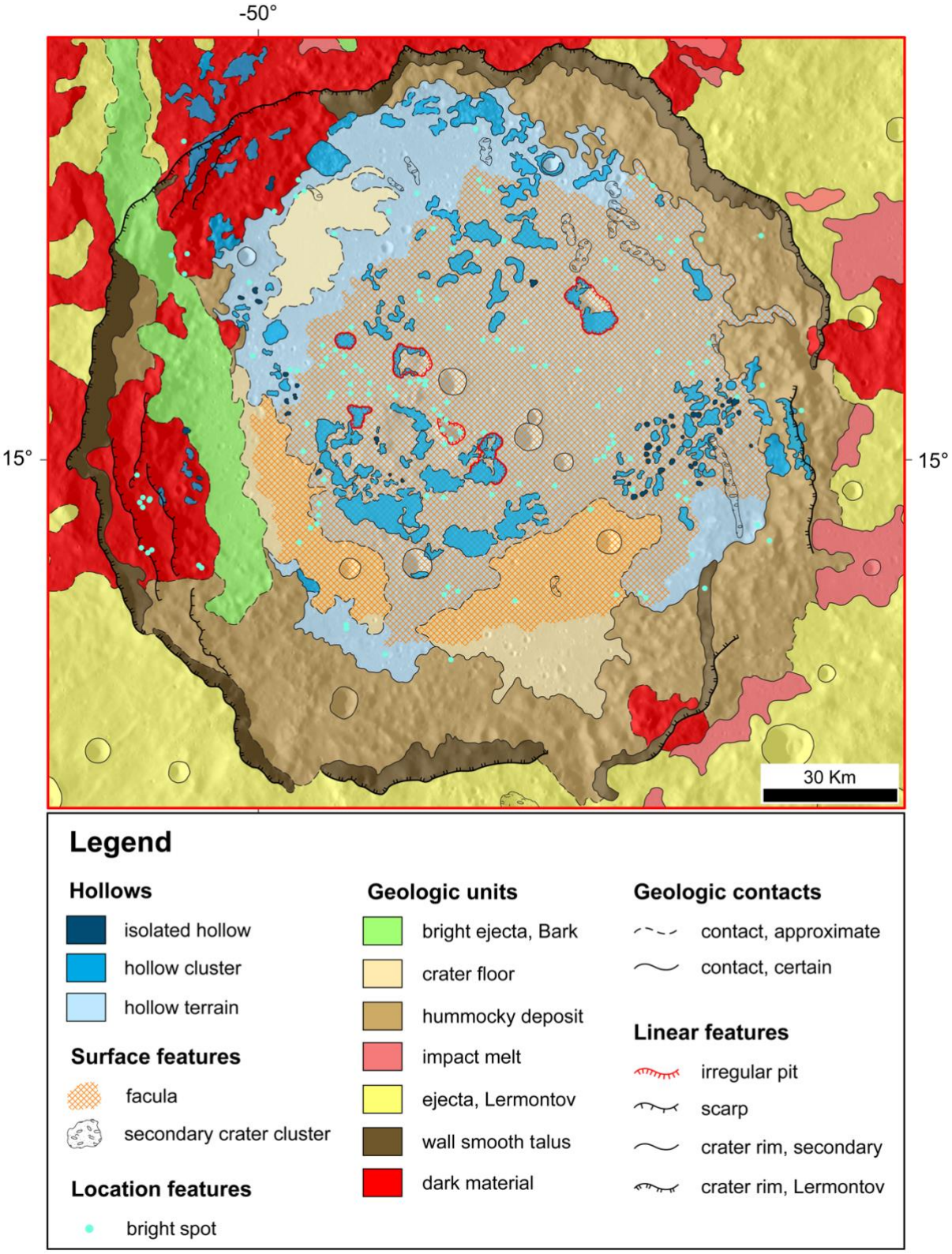

Figure 12. A close up view of the geological map, focusing on the geologic units located in the inner part of Lermontov crater.

The crater floor appears strongly affected by hollow-related morphologies and deposits, which cover almost entirely the flat area inside the crater, and also some portions of the crater wall and ejecta (in the northern sector). Hollow deposits are mapped following the same classification adopted within previous works (Lucchetti et al., 2018), distinguishing 'isolated hollows', 'hollow cluster' and 'hollow terrain'. These units identify, respectively, single depressions that are tens or a few hundred meters large; wider depressions with irregular boundaries linked together, forming irregular sunken areas that range, in this area, from hundreds of meters up to tens of kilometres in width; high-albedo areas, with hollow-related morphologies, containing and surrounding scattered hollows that are too small to be individually mapped. In some cases, point features such as 'bright spots' were needed to identify high-albedo small features, that are likely to be associated with isolated hollows, but with no clear morphology and therefore not distinguishable as a superficial unit. We recall that given the spatial scale of the NAC images available in this area, all hollow-related features were mapped at a scale between 1:60.000 and 1:100.000.

Moreover, analysing false-colour WAC images, in particular the MD3-color, and the MDIS Enhanced-color (with the colour normalized Brovey sharpening technique applied) it was possible to recognize other superficial units, based on their spectral composition (different false colours are associated with different composition of the material on the surface). The Lermontov crater, indeed, appears to be cross-cutted by a bright ray of high-albedo material, which is attributed to the ejecta deposits of the Bark crater, located ~250 km north of the Lermontov crater[4]. These bright rays, mapped as a separate unit, cover part of the Lermontov ejecta deposits in the northern sector and cross-cut the crater itself in the western part, resulting in a well-distinguishable stratigraphic marker, younger than the Lermontov impact event and

[4] The Bark crater is a ~35 km wide crater on Mercury that formed during the Kuiperian age. Its rays can extend up to 550-600 km from its center.

its related geologic units. Furthermore, a consistent portion of the Lermontov ejecta deposits, mostly in the north-western sector, is characterised by a distinctive dark colour (dark blue in the MDIS false-colour images), which is likely to be associated with a Low-Reflectance Material (LRM) component in the excavated material after the impact event. Thus, this material was mapped as 'dark material'.

Another important feature, identified within the crater floor, is an unnamed *facula* (i.e., a bright spot, usually associated to pyroclastic deposits on Mercury, Kerber et al., 2011), which covers almost entirely the crater floor in the central and eastern portion, but it appears to be older than hollows deposits (which are found, therefore, on top of this *facula*). This deposit is undetectable within the NAC images and not visible in the monochrome global basemaps, but its boundaries are well recognizable in the MDIS colour basemaps, and in particular in the Enhanced-colour mosaic. All "colour" units have been mapped at an average scale of ~1:400.000.

Modelled chronology

By means of the geological map of Fig. 12, we outlined and quantified the extension of Lermontov's floor, which is 12984.4 km^2 (Fig. 13A). Inside this unit, we identified 456 craters with sizes $\geq$ 0.3 km (with a maximum detected size of 6.9 km), not considering those that are secondary clusters, as well as those located inside the Bark crater ejecta rays (Fig. 11). We then carried out the statistical analyses of the craters and the crater modelled retention age of the Lermontov floor using the software "Craterstats 2" (http://hrscview.fu-berlin.de/craterstats, Michael and Neukum, 2010; Michael et al., 2012; Neukum, 1983). We used both the production functions (PF) and chronology functions (CF) of Neukum et al. (2001) and of Le Feuvre and Wieczorek (2011) in order to evaluate if there are any possible differences among the two chronology systems (Fig. 13 B and C).

311 Blewett et al. (2013), as well as Goudge et al. (2014) described Lermontov as a crater of
312 Mansurian age, i.e. with an emplacement time ranging from 3.5/3.0 to 1.0 Ga if the Spudis and
313 Guest (1988) time-stratigraphic system is considered, from 1.70 to 0.28 Ga if Marchi et al.
314 (2009) model production function is considered, or from 0.85 to 0.13 Ga when the Le Feuvre
315 and Wieczorek (2011) stratigraphic-age is used. Instead, as Fig. 13 B and C show, our modelled
316 age range from 3.84 $\pm$0.01 Ga when the PF and CF of Neukum et al. (2001) are used, to 3.74
317 $\pm$0.01 if the PF and CF of Le Feuvre and Wieczorek (2011, porous case) is considered.

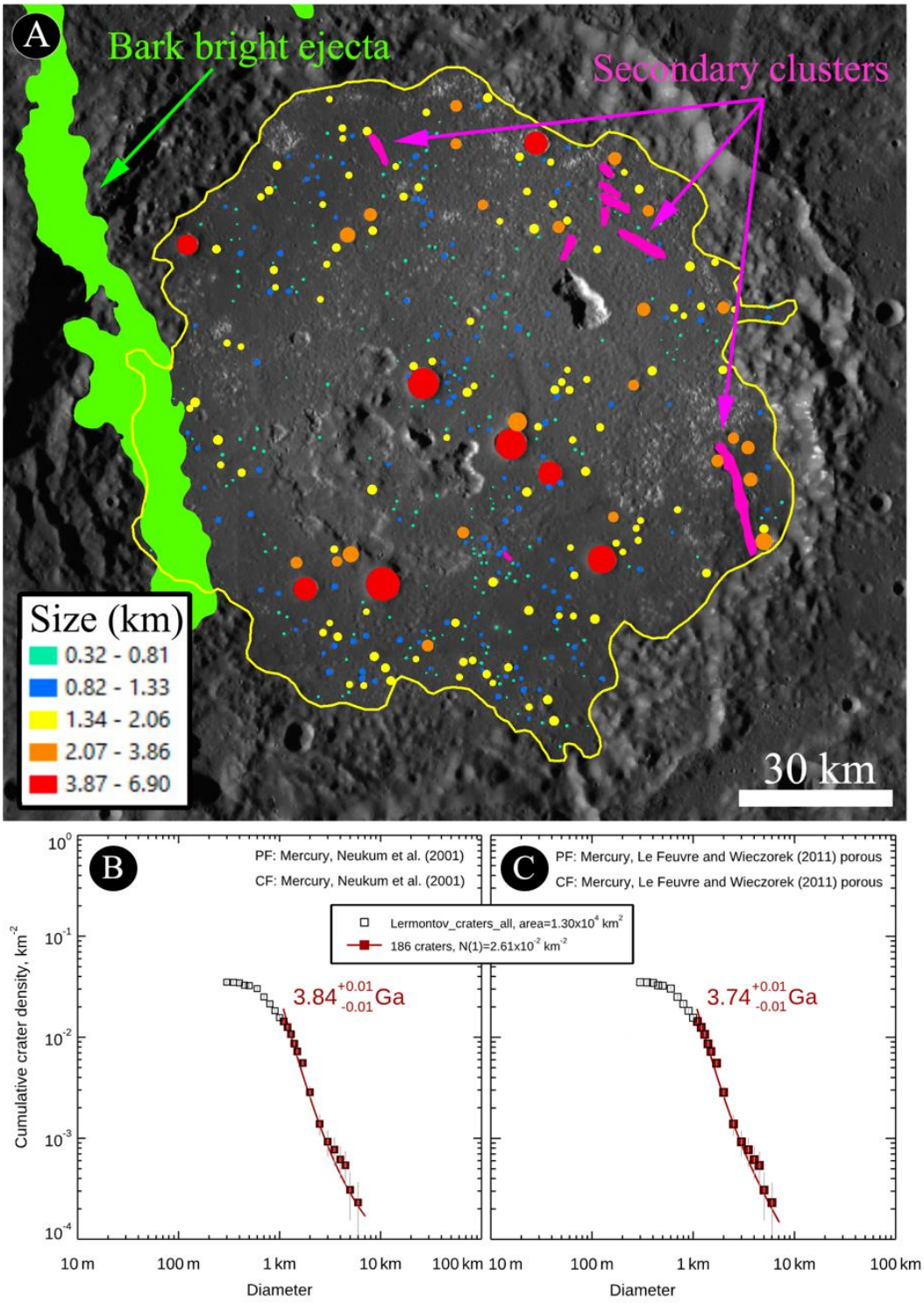

Figure 13. A) The Lermontov floor area (12984.4 km2), outlined in yellow, where we counted all craters ≥ 0.3 km, excluding both secondary clusters (pink), as well as the Bark crater ejecta rays (green). B) The modelled age of Lermontov floor as computed through Craterstats 2, when considering the PF and CF of Neukum et al., 2001. C) The modelled age of Lermontov floor when considering the PF and CF of Le Feuvre and Wieczorek (2011) porous case.

Spectrophotometry and Clustering

The four selected areas where we focused and applied the spectral clustering technique are presented in Fig. 9:

- Selection 1 is located in the south-west pyroclastic deposit and includes multiple irregular pits. By using the clustering technique, a natural number of eight clusters is identified (Fig. 14A). Each resulting cluster is characterised by its average and associated standard deviation: all spectra are then normalised at 0.56 μm to evaluate their mutual differences. Clusters number from 0 to 4 are typically associated to the pyroclastic deposit (with cluster no. 2 being the steepest/reddest one). Instead, clusters no. from 5 to 7 are associated to the bright rims of the pits (cluster no. 7 is the shallowest/bluest one);
- Selection 2 covers the north-east Lermontov pyroclastic deposits and it includes the NE vent. Here eight clusters are identified[5] (Fig. 14B). Clusters from no. 0 to 3 cover the red, pyroclastic deposit, with cluster no. 2 being the one with the reddest spectral behavior, as well as covering the largest surface of the studied area. Instead, clusters no. 4 and 5 encompass the innermost part of the vent. Clusters 6 and 7 almost entirely locate in the vents rim and show the shallowest trend (cluster no. 7 is the one presenting the bluest spectral trend among all spectra);
- Selection 3 lies on the hollow clustered area situated in the central-east part of Lermontov floor (we hereafter call such hollows "field hollows"). A natural number of 11 clusters is identified here (Fig. 15A). The clusters with numbers from 0 to 3 are all located in the easternmost part of the selection, where the presence of hollows is sparse; on the contrary clusters 4 and 5 cover the west-central part of the study area, where the

[5] We recall that finding an equal number of clusters for the first two selections is a random result because the process is unsupervised.

red pyroclastic deposits occur. Cluster no. 5 is the one showing the steepest trend. Clusters 6 and 7 mostly surround the hollow clusters as well as isolated hollows, and show a flatter spectral behaviour than the previous ones. Clusters from 8 to 10 are, instead, entirely located inside the hollows and present the bluest trend, with cluster 10 being the shallowest one;

- Selection 4 is located ~50 km far from Lermontov crater's rim, inside the ejecta deposits. A natural number of eight clusters are here identified, all presenting a similar (Fig. 15B), red trend as the wavelength increases from 0.4 to 1.05 μm. The shallowest cluster is no. 7, while the steepest one is cluster no. 0.

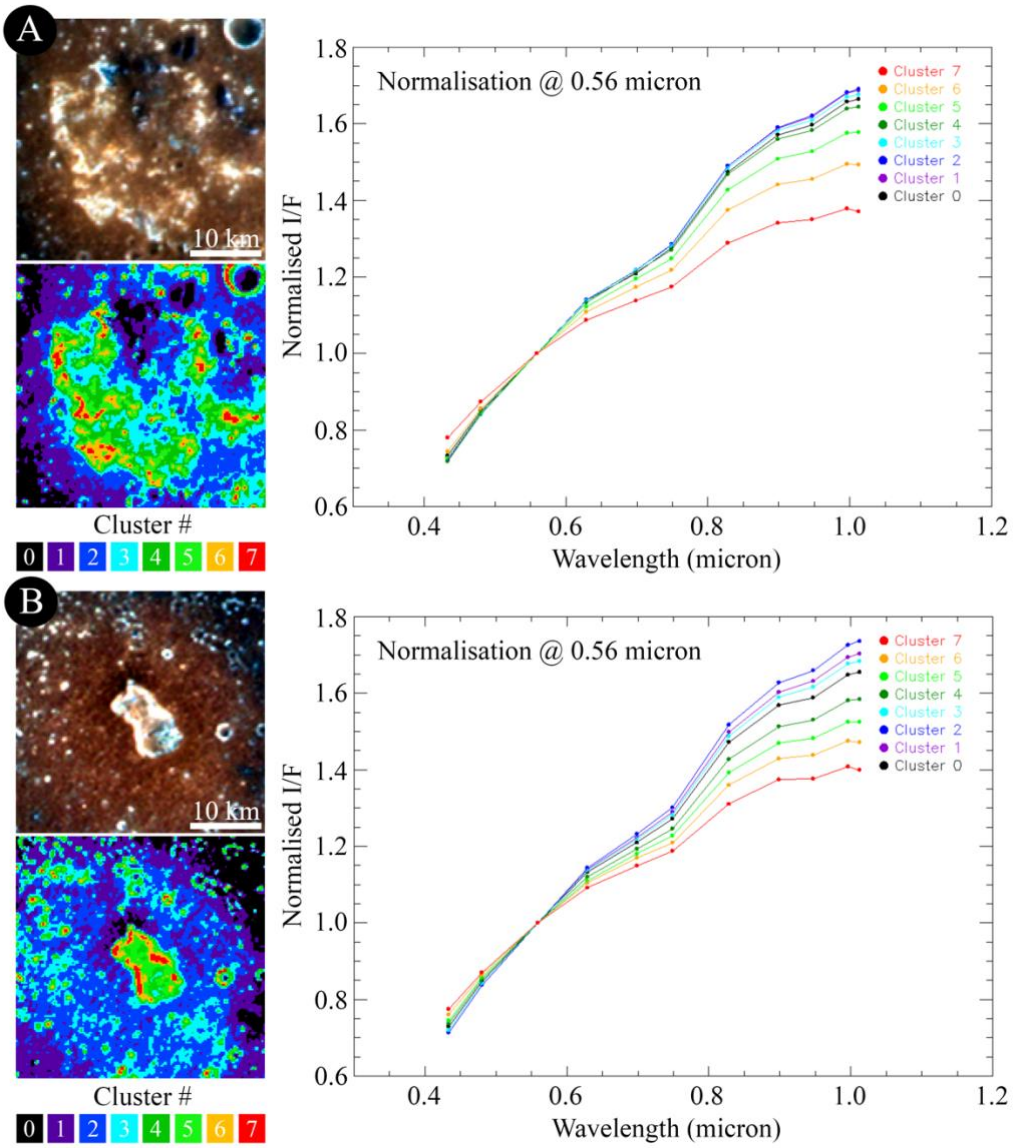

Figure 14. A) Selection 1 (150 × 150 pixels) where we applied the clustering technique. The RGB image was prepared using filter at 1.012 μm for the red channel, filter at 0.698 μm for the green channel and filter at 0.433 μm for the blue channel (this configuration is used for all, following selections). The spectra obtained for all clusters are normalised at 0.56 μm). B) Selection 2 (150 × 150 pixels) returns 8 clusters as the natural number and it is centred on Lermontov NE vent.

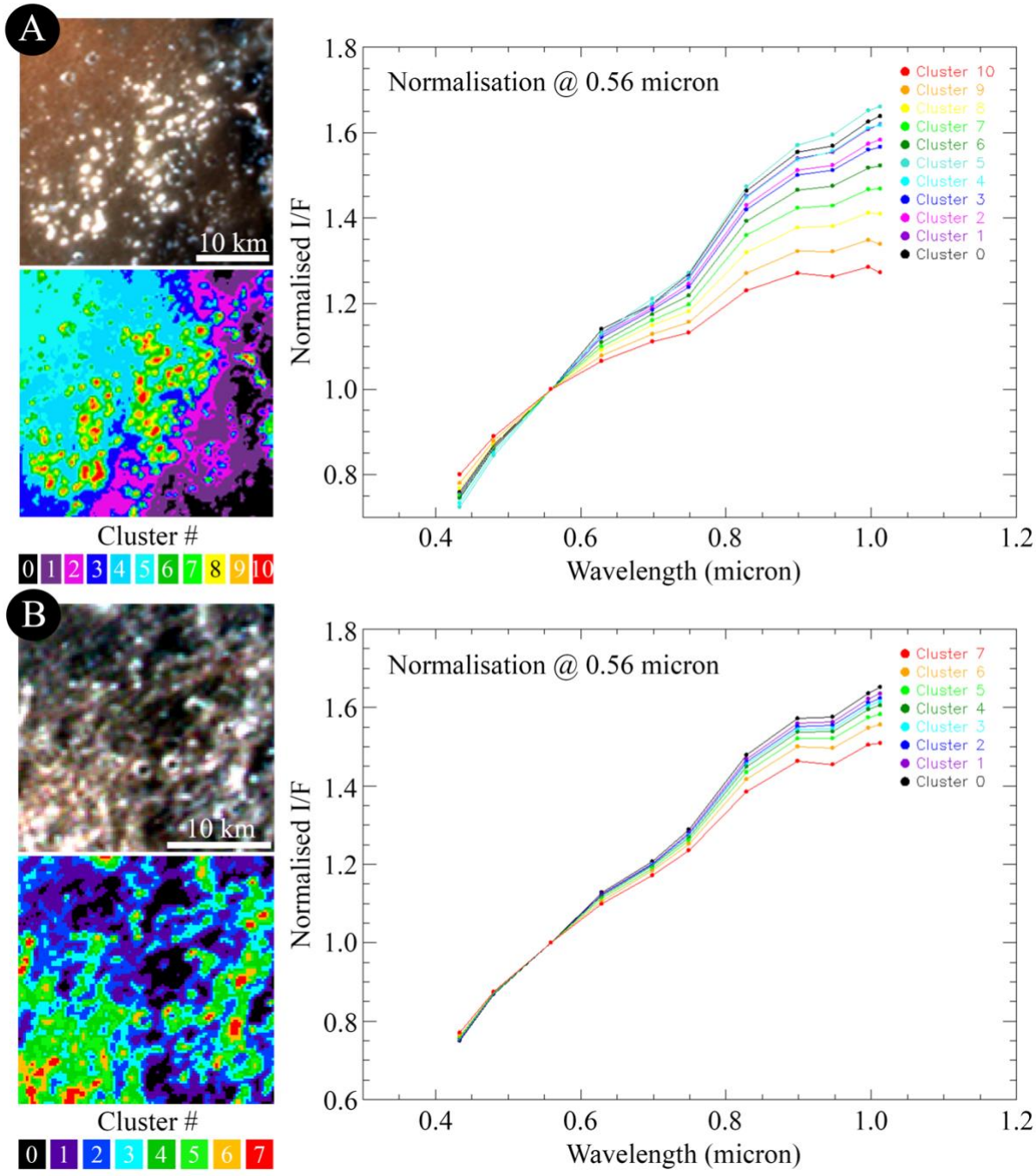

Figure 15. A) Selection 3 (150 × 150 pixels) where we applied the clustering technique, together with the RGB image and the 11 clusters identified. The spectra obtained for all clusters are normalised at 0.56 μm). B) Selection 4 (100 × 100 pixels) returns 8 clusters as the natural number and it is located in the Lermontov ejecta deposits.

Discussion

The Lermontov crater floor is characterised by two pyroclastic deposits: the NE one is centred at 15.1° latitude, and -49.2° E longitude, while the SW one is centred at 15.8° latitude, and -48.2° E longitude. Using both a stretched MDIS-WAC RGB image and a color-normalised Brovey sharpening of the Enhanced-color basemap of the crater (Fig. 16A, B), we have been able to quantify the extension of the two deposits, deriving an area of ~ 3800 km^2 for the NE one, and ~ 4800 km^2 for the SW one. This results in sizes ranging between 34 and 36 km for the NE deposit, and between 37 and 41 km for the SW one, comparable to other measured pyroclastic deposit sizes on Mercury (Kerber et al., 2011). A previous analysis done on MESSENGER flybys 1-3 images (Kerber et al. (2011) suggested that the NE and SW deposits could be 33 and 31 km, respectively. Nonetheless, as the geological map (the facula extension in Fig. 12) and the red arrows of Fig. 16A highlight, the transition region between the red deposits and the surrounding units might be slightly larger. If we assume a size of 35 km for the NE deposit, and 39 km for the SW one and we insert them in Eq. 1 of Kerber et al. (2009), we can estimate the required vent eruption speed (v_e) as a function of the ejection angle (θ), to reach these maximum dispersal distances (Table 1).

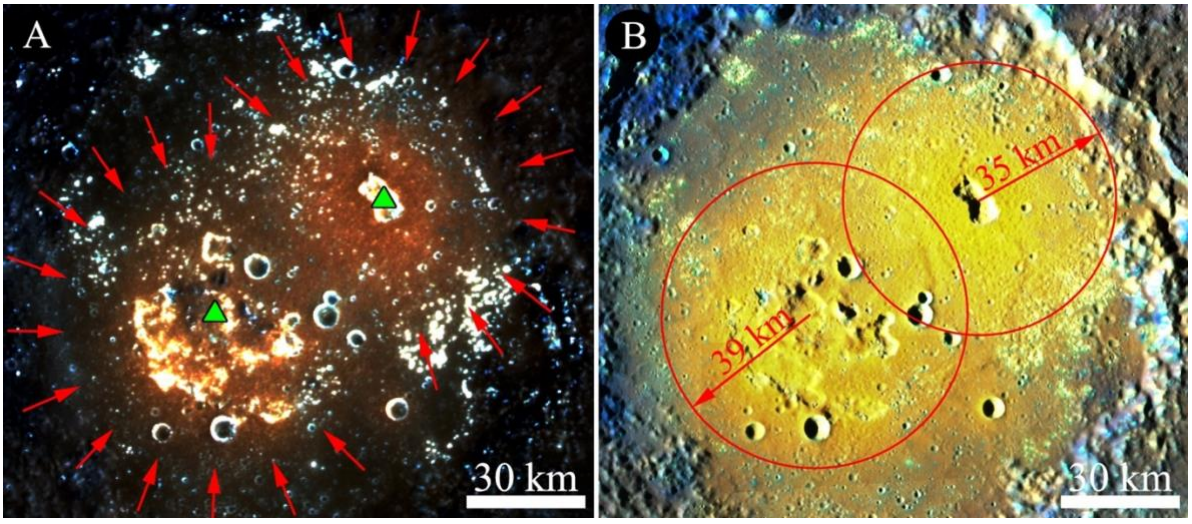

Fig. 16. A) Stretched RGB image, as of Fig. 1C, to highlight the extension of the two pyroclastic deposits (red arrows) identified on Lermontov floor. The two vents are indicated with the green triangles and their mutual

distance is 52 km. B) Color Normalised Brovey Sharpening of the Enhanced-colour basemap of Lermontov. The SW and NE pyroclastic deposits are highlighted with red circles, together with their radial extension of 39 km and 35 km, respectively.

Deposit	**Lermontov NE**	**Lermontov SW**
Area (km^2)	~3800	~4800
Radius (km)	35	39
θ = 45° - Velocity (m/s)	360	380
θ = 30° - Velocity (m/s)	387	408
θ = 15° - Velocity (m/s)	509	537
θ = 7.5° - Velocity (m/s)	707	747

Table 1. The required vent eruption speeds v_e, computed in m/s at different angles of ejection θ (measured from the zenith) to reach Lermontov NE and SW maximum dispersal distances.

Since during a hermean eruption there is no atmospheric drag dissipating its energy (Mercury is an atmosphereless body), the clasts ejected from the vent only interact with the volcanic gas entraining them (Wilson and Head, 1981). Such gas quickly decompresses to the point where gas-particle interactions become negligible, leaving the pyroclasts to follow ballistic trajectories back to the surface[6] (Head and Wilson, 1979; Wilson and Keil, 1997, Kerber et al., 2011). For this reason, the maximum dispersal of pyroclasts takes place at θ equal to 45°, resulting in a minimum v_e (a smaller or larger ejection angle θ would need a greater v_e in order for the pyroclasts to reach the maximum dispersal distance, Table 1). By considering the gravitational acceleration at the surface of Mercury, g_{Merc}, of 3.7 m/s^2, we derive a minimum v_e of 360 m/s for the Lermontov NE deposit, while a minimum v_e of 380 m/s for the SW one.

[6] An explosive eruption on a planet without atmospheric pressure also leads to a more widespread dispersal because the expanding gas goes from its initial pressure in the vent to a zero-external pressure.

In addition, Kerber et al. (2011) presented the required magmatic abundances (in parts per million, ppm) of different volatile species that could be needed to eject a pyroclastic particle to a specific distance of Mercury[7]. The selected volatiles are those commonly encountered on Earth, such as carbon monoxide (CO), water vapour (H_2O), carbon dioxide (CO_2), sulfur dioxide (SO_2) and hydrogen sulfide (H_2S). However, since the reduced and dry conditions of Mercury's magmas imply gas speciation that is dissimilar to Earth's volcanic gases, Zolotov (2011) highlighted through chemical equilibrium models that nitrogen gas (N_2), CO, sulfide (S_2), carbon disulfide (CS_2), disulfur chloride (S_2Cl), chlorine (Cl), chlorine gas (Cl_2) and carbonyl sulfide (COS) may be among the most abundant volcanic gases of the planet[8]. Given that the volatiles triggering the hermean pyroclastic explosions are still largely debated, we decided for this work to consider both Kerber et al. (2011) as well as Zolotov (2011) lists to estimate the magmatic abundances required to emplace pyroclastic material to the radial extent of the two Lermontov deposits (Table 2).

On Earth the amount of volcanic gases such as H_2S and SO_2 measured at the vent varies between 10000 and 100000-250000 ppm, respectively, while for CS_2 or COS it may range between 1 and 100 ppm (Textor et al., 2003). For CO_2, this value can change between 10000 and 400000 ppm, while for water vapour it can be as high as 900000. With the exception of H_2O[9], the amount of magmatic gases of Table 2 is comparable to (lower limits for CO_2, H_2S and SO_2), if not exceeding (CS_2 or COS) the quantity of volatiles detected at terrestrial vents. Therefore, regardless of the volatiles' mixtures that may have triggered the pyroclastic explosions inside Lermontov, this supports the interpretation of Kerber et al. (2009, 2011) and Asphaug and Reufer (2014) that the hermean crust is not as extremely depleted in volatile

[7] The volatiles driving pyroclastic eruptions depend on the starting composition of the accreted planet, the redox state of the mantle, as well as the pressure and temperature conditions occurring while the erupting magma rises, hence affecting how the volatile components partition into the gas phase, Zolotov (2011).

[8] Zolotov (2011) suggested that species as S, Cl and N could survive planetary devolatilisation events because they are stale in their solid, reduced forms.

[9] We recall that for Kilauea volcano in Hawaii a value of 3000 ppm of H_2O is measured, Gerlach, 1986.

437 materials as it was suggested by different models of volatile depletion (Boynton et al., 2007),
438 such as disruption due to a giant impact (Wetherill, 1988; Benz et al., 1988, 2007) or
439 vaporisation of the crust in the hot nebula (Fegley and Cameron, 1987).
440 From a spectral perspective, by applying the clustering technique to the Lermontov SW (Sel.
441 1) and NE deposit (Sel. 2), we identified that clusters no. 2 of both selections are the ones
442 associated to the pyroclastic material situated in closest proximity to the vents. The comparison
443 between the geological and the clustering map (Fig. 17A-D) reveals indeed that the reddest
444 spectra are associated to the pyroclastic bright facula. Moreover, if we compare the two
445 spectrophotometric behaviours (Fig. 17E) we note that they both overlap within the 1σ range,
446 supporting the interpretation that the two pyroclastic deposits are spectrally similar. An alike
447 surficial spectrophotometry may suggest that the two magmatic chambers supplying the vents
448 have had a similar composition, though their different sizes. An alternative hypothesis might
449 be that instead of two volatile reservoirs, there could be a single, bigger magmatic chamber that
450 may have alternatively fed both vents, hence resulting in a similar ejected composition.
451

Volatile	**Lermontov NE**	**Lermontov SW**
CO	8100	9000
H_2O	5200	5800
CO_2	12700	14100
SO_2	18600	20600
H_2S	9900	11000
HCl	10500	11700
N_2	8100	9000
S_2	18500	20600

CS_2	22000	24500
S_2Cl	28800	32000
Cl	10300	11400
Cl_2	20500	22800
COS	17400	19300

Table 2. Volatiles magmatic abundances in part per million as from Kerber et al. (2011) and Zolotov (2011), computed to emplace pyroclastic material to the maximum radial extent of Lermontov NE and SW deposits.

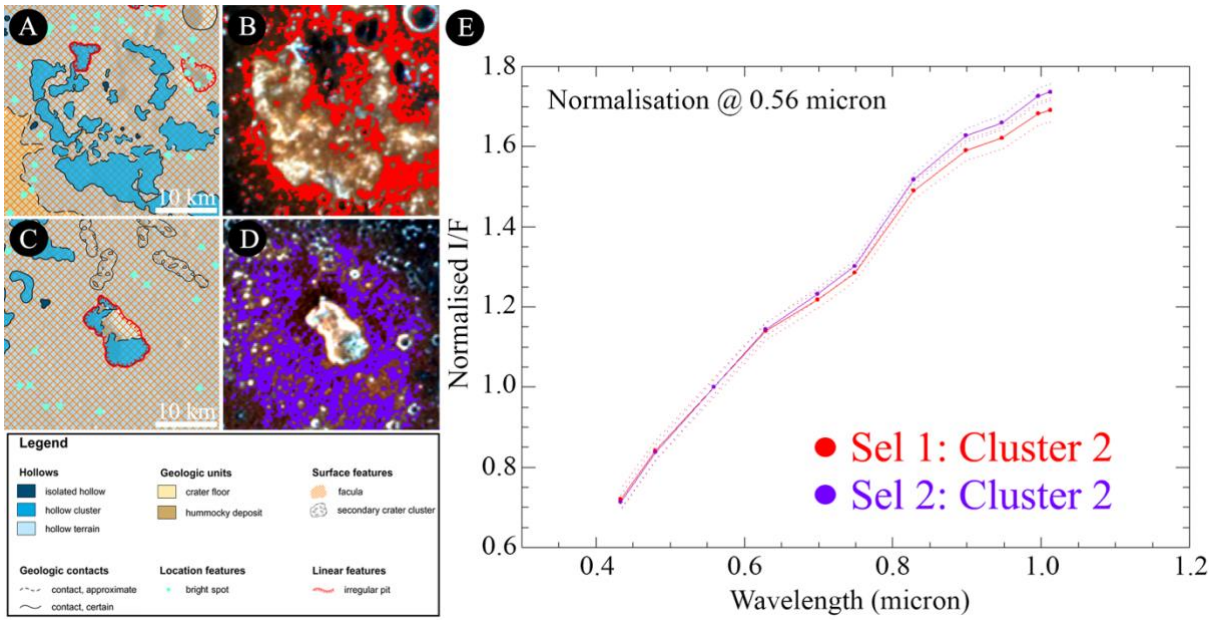

Fig. 17. A) Geological map closeup of Sel. 1. B) Clustering map on top of the RGB of Fig. 14A showing the extension of cluster no. 2. C) Geological map closeup of Sel. 2. D) Clustering map on top of the RGB of Fig. 14B showing the extension of cluster no. 2. E) Normalised I/F for the two clusters no. 2 extracted from Sel. 1 and 2. The dotted lines show the 1σ range for each spectrum.

Since we do not quantitatively know the thickness of the pyroclastic deposits on Lermontov (and hence the full obliteration and coverage of all craters emplaced before the vent explosions), there may be a chance that the derived modelled age (3.84-3.74$\pm$0.01 Ga) is the one of the red

466 deposits themselves. If this is the case, the pyroclastic deposit age can be considered only as an
467 lower limit for the Lermontov emplacement itself. On the contrary, if this is not the case, the
468 modelled age we obtained can be attributed to the crater floor before the pyroclastic
469 emplacement. For both cases, this suggests that Lermontov crater emplacement is much older
470 than previously highlighted (Blewett et al. (2013), Goudge et al. (2014)), falling in the Late
471 Tolstojan/Calorian timeframe (Spudis and Guest, 1988; Marchi et al., 2009; Le Feuvre and
472 Wieczorek, 2011).
473

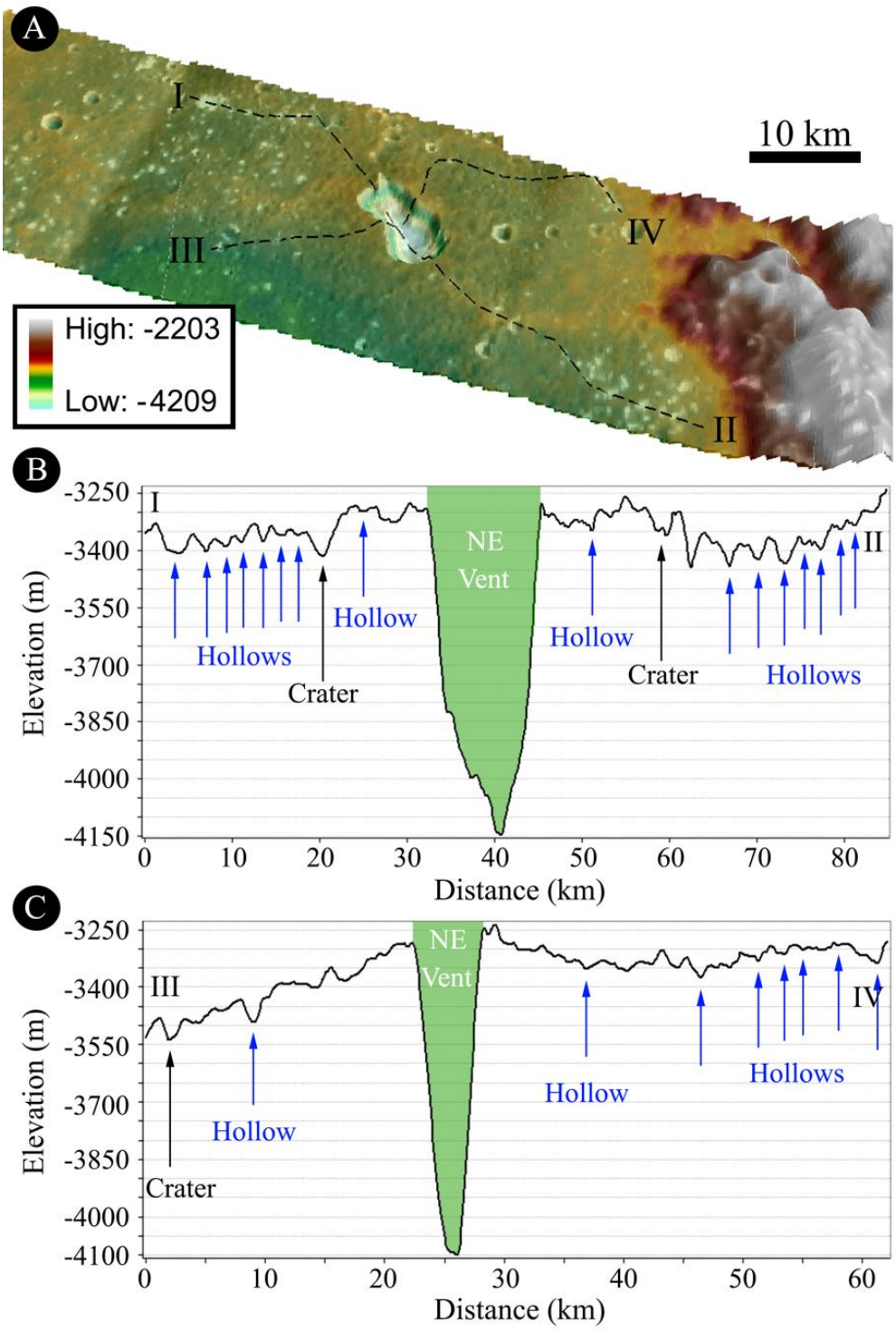

Fig. 18. A) 3D representation of the Lermontov NE vent and its closest surroundings. Elevation values are in m. Profiles I-II and III-IV are indicated on the DTM. B) Profile I-II showing the location of different hollows (blue arrows), craters (black arrows) and the Lermontov NE vent (longest dimension). C) Profile III-IV showing the location of different field hollows (blue arrows), craters (black arrows) and the Lermontov NE vent (shortest dimension).

The high resolution DTM published by Fassett (2016) covers the central-north part of the crater (Fig. 18A), and it returns an exhaustive representation of Lermontov NE vent and its closest surroundings with a spatial scale of 155 m and a vertical scale of few tens of m. The measured area of the vent is 81.2 km^2, with a length ~12.5 km and a width spanning from 5 to 8 km. Such dimensions are comparable to other hermean vents (Table 1 of Kerber et al., 2011 shows length values ranging 7-38 km and widths spanning 4-28 km) but also to lunar vents resulting from explosive volcanic activity (Head et al., 2002). The maximum depth of the vent is instead ~ 0.95 km (Fig. 18B), which is shallower than the 1.2-2.4 km range obtained by Goudge et al. (2014) on six vents, but it is 0.15 km deeper than the Praxiteles crater vent (which present a comparable length of 13 km to the Lermontov one, Fassett, 2016). By exploiting Fassett (2016) DTM it is also possible to analyse the field hollows' dimensions (Fig. 18B and C) and compare them with the nearby vent. Hollows are shallow pits that generally do not exceed depths of 50-100 m (Blewett et al., 2011; 2013): as profiles I-II and III-IV highlight, Lemontov field hollows confirm this trend presenting maximum depths of 70-80 m, i.e. they are "surficial" features that are 10-15× shallower than the proximal vent.

Through the use of the MDIS-NAC high-resolution mosaics prepared for the geological mapping, we have identified hollows not only in the pyroclastic deposit located on the crater floor (field hollows), but also inside the SW and NE vents, particularly close to their rims (Fig. 19A-C for the SW vent, Fig 19D for the NE vent).

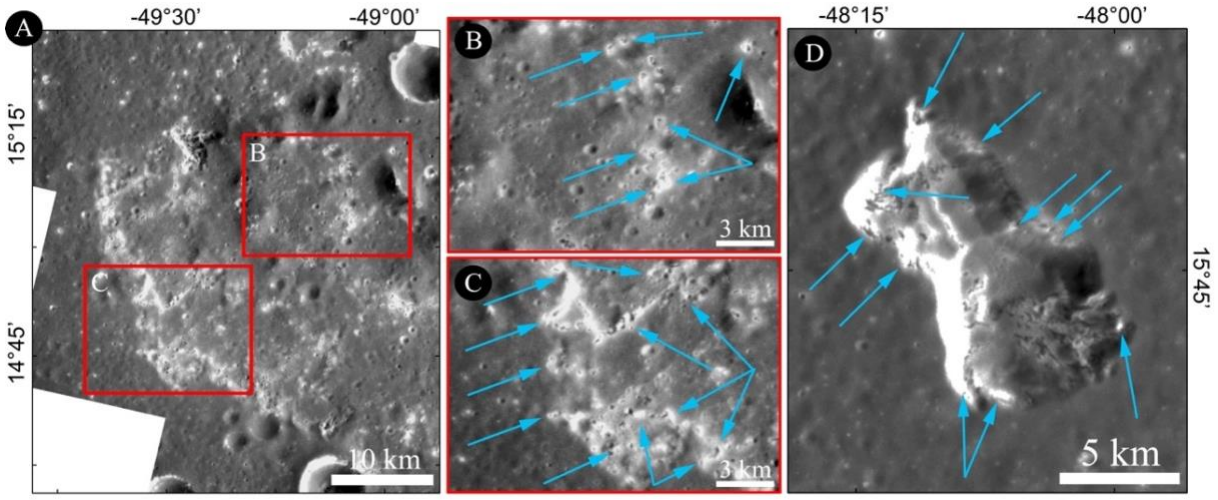

Fig. 19. A) High resolution mosaic showing the SW Lermontov vent. B) and C) are close-up views showing the presence of hollows (light blue arrows) inside the vent rims. D) High resolution mosaic showing the NE vent and the occurrence of hollows, indicated with light blue arrows. Note the different degradation states of the two vents (as previously highlighted by Goudge et al., 2014): the NE vents shows crisp edges, while the SW one has much more degraded edges.

Despite a 5× to 10× coarser spatial scale of the multiband WAC dataset with respect to the NAC one, the clustering technique is able to separate such "vent hollows" from their surrounding terrains, hence returning their spectral behaviour. Fig. 20A-D shows the presence of the vent rim hollows, that appear both in the geological close-up as well as in the clustering map. As it is possible to see both hollows of the SW vent and those of the NE one are characterised by a similar trend, within the 1σ range. If we then compare these hollows with the field ones (Sel. 3, Fig. 20E, 20F) we find that the vent hollows generally present a steeper spectral slope than the field hollows. This could be a consequence of their slightly different mineralogical composition.

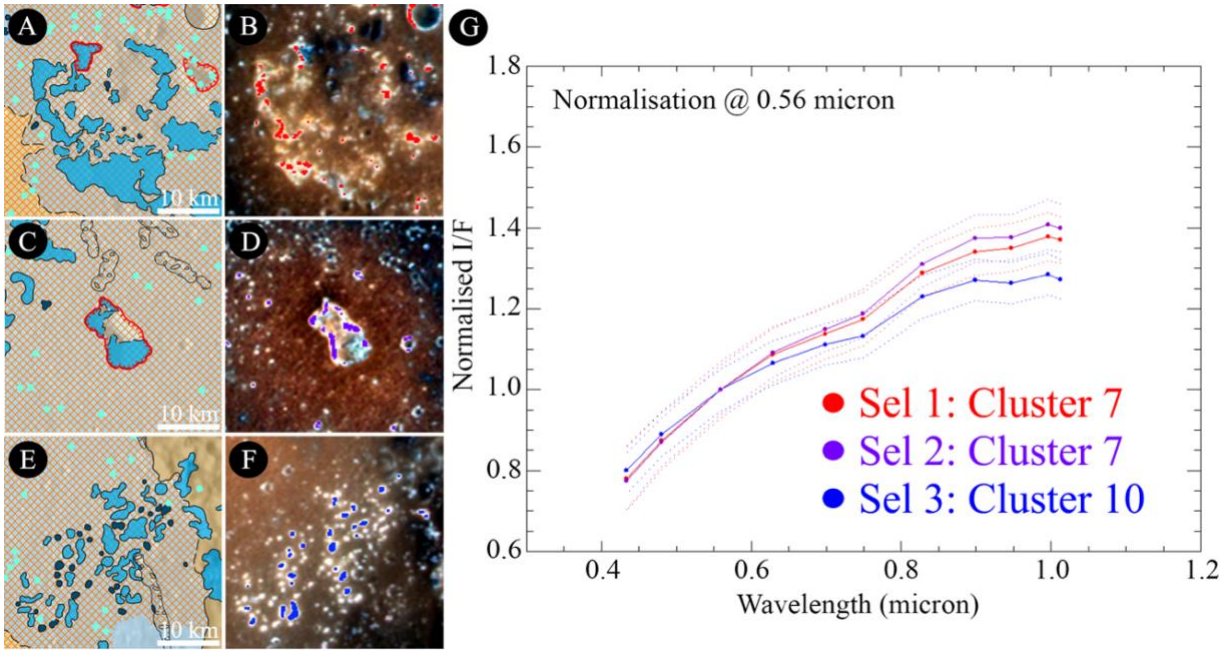

519

520

521 Fig. 20. A) Geological map closeup of Sel. 1. The legend is the same of Fig. 17. B) Clustering map on top of the
522 RGB of Fig. 14A showing the extension of cluster no. 7. C) Geological map closeup of Sel. 2. D) Clustering map
523 on top of the RGB of Fig. 14B showing the extension of cluster no. 7. E) Geological map closeup of Sel. 3. F)
524 Clustering map on top of the RGB of Fig. 15A showing the extension of cluster no. 10. G) Normalised I/F for the
525 two clusters no. 7 extracted from Sel. 1 and 2 and of cluster no. 10 extracted from Sel. 3. The dotted lines show
526 the 1σ range for each spectrum.

527

528 Several mineralogical candidates have been proposed to interpret the hollows spectra. Ca and
529 Mg are the most common elements cited for the relatively volatile material (Blewett et al., 2011;
530 Helbert et al., 2013). Recently, Lucchetti et al. (2018) suggested the presence of a mixture of
531 different silicate minerals (sulfides and silicates with different relative abundances) may
532 contribute to the absorptions found in our spectra. In particular, they proposed Ti-rich pyroxene,
533 Cr-rich pyroxene and Ni-rich pyroxene as plausible end-members to model hollows
534 composition. Following this line of research, we selected multiple types of pyroxenes with

enrichment of different elements[10]. In addition to what done previously, we added for this work a V-rich pyroxene from Cloutis (2002) because it is one of the pyroxene transition series elements that is frequently found as a substitute for Fe in magnetite and in the ferromagnesian silicate minerals formed during magmatic processes (Curtis 1964). When focusing on the volatile compounds, Lucchetti et al. (2018) selected MgS, MnS and CaS, that are three thermally altered sulfides from Helbert et al. (2013). Since Zolotov (2011) suggested that chloride compounds may also be constituents of Mercury mantle and magmas, we decided to add to our dataset three RELAB samples of MgCl (C1WV01), CaCl (BKR1JBG29B) and $FeCl_3$ (CALW01).

In the four-representative cluster spectra of Lermontov (Fig. 21) some spectral features are still recognizable, despite a not so high spectral contrast. A broad band located between 0.63 μm and 0.83 μm seems to be present in all the spectra. A hint of band at 0.95 μm clearly appears in the spectrum of the outer terrain cluster (this is the ejecta deposits mean spectrum of Sel. 4) and, with less spectral contrast, in the spectrum of both field and vent hollows.

[10] To exclude possible effects due to the peculiarities of the sample that could influence the matching process, we mediated all samples containing the same element (Cloutis, 2002). Therefore, PYX018, PYX153 and PYX170 (all catalogued as Cr-rich pyroxene) were averaged to obtain a representative spectrum of the class of mineral. The procedure has been repeated for Mn- and Ti-rich pyroxene. Original spectra from Cloutis (2002) and the average spectra evaluated in our work are reported in SM Figure 1. Following Lucchetti et al. (2018) we also selected Ni-rich pyroxene from White et al. (1971).

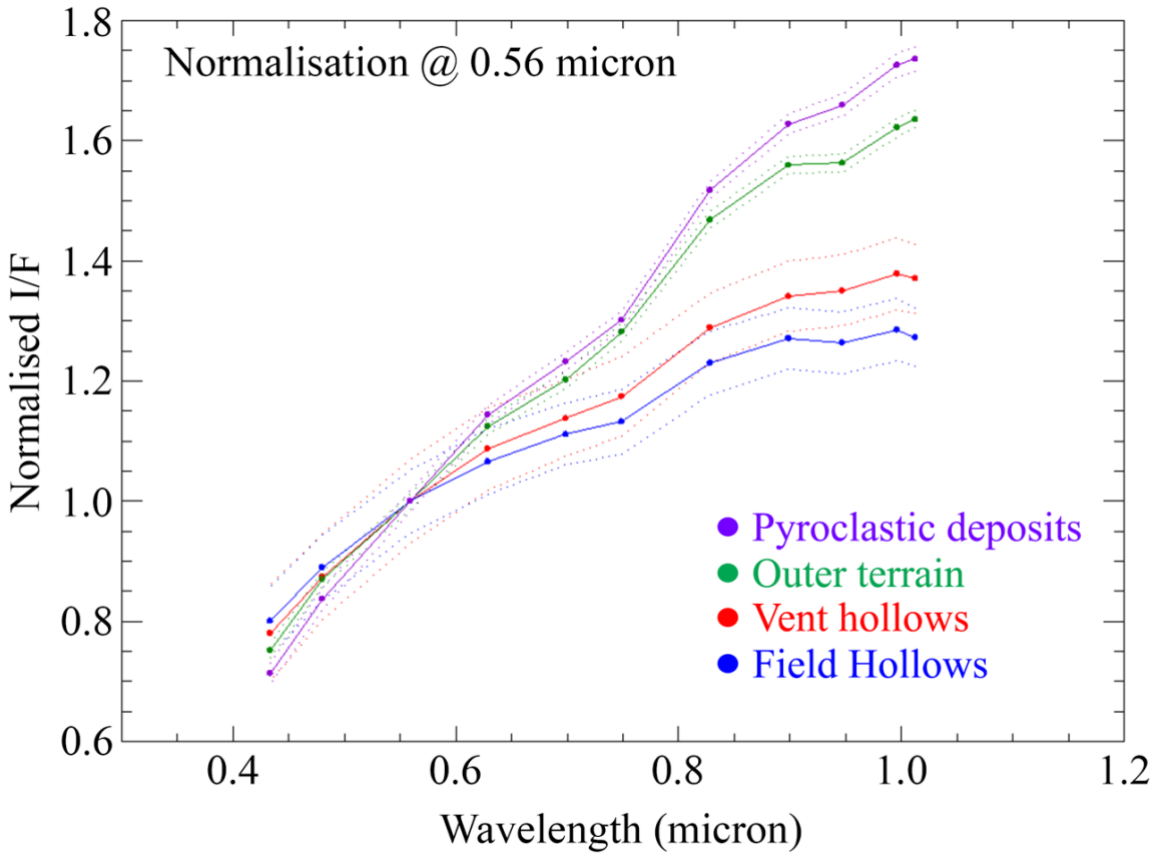

Fig. 21. The representative cluster spectra of Lermontov are taken from Fig. 17E (pyroclastic deposits), Fig. 20G (vent hollows and field hollows) and Fig. 15B (outer terrain).

End member spectra with a wide band between 0.6 µm and 0.8 µm are Ni-rich, Ti- rich and V-rich pyroxene, as visible in Fig. 22B. On the contrary, sulfides and chloride have smaller bands that are not closely related to the broad band observed in the Lermontov spectra (Fig. 22C, D). For this reason, we can infer that the crater region might spectroscopically be dominated by the presence of a mix of various pyroxenes with different compositions and, in particular, containing Ti, Ni and possibly Vanadium. Instead, the hint of band at 0.9 µm is not typical of pyroxene, which is usually characterised by a broader band around 1 µm.

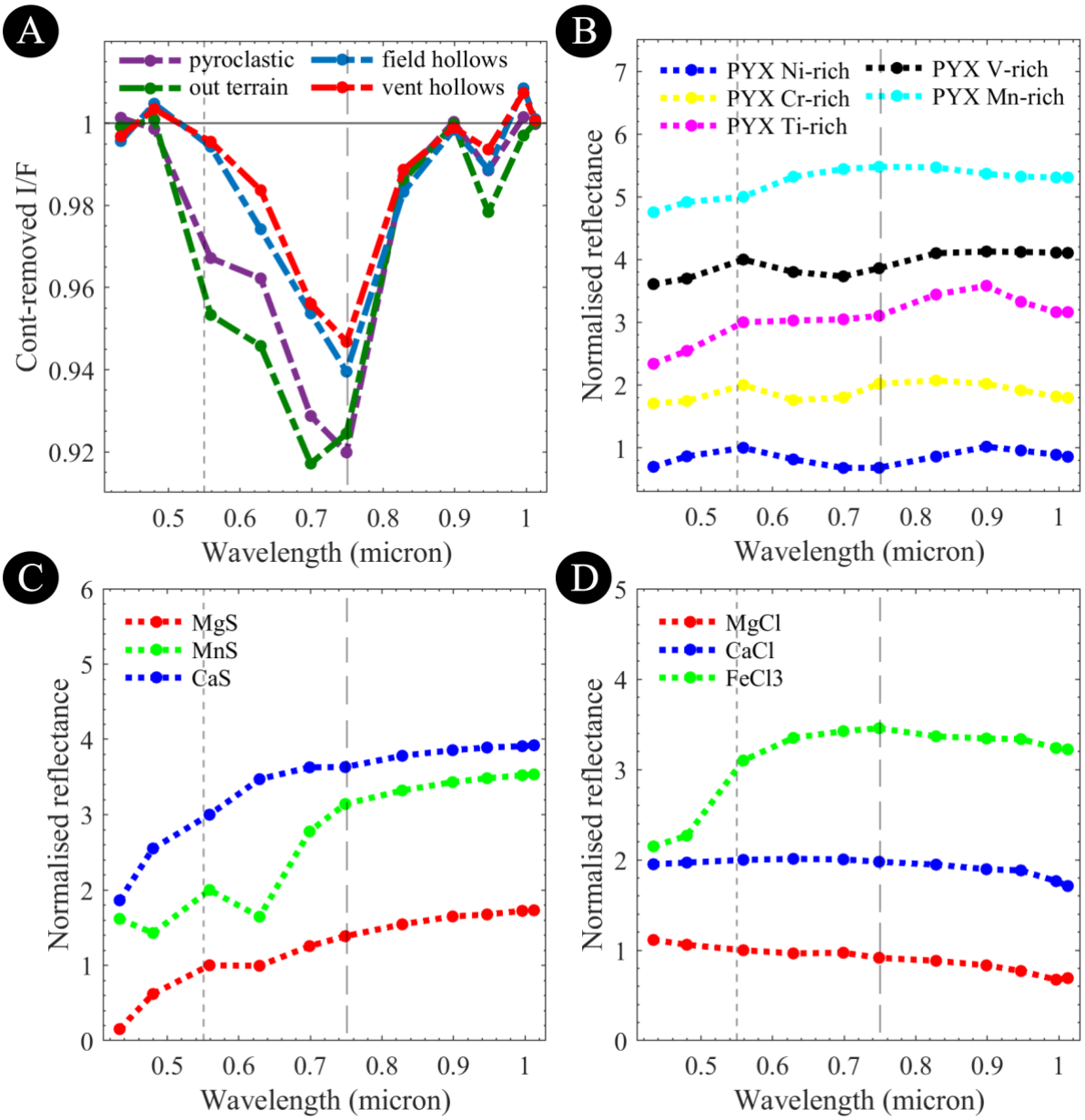

Fig. 22. A) The representative cluster spectra, continuum-removed, for four the different features identified on Lermontov crater: the pyroclastic deposit, the "outer terrain", i.e. the ejecta deposits of Sel. 4, the vent hollows and the field hollows located in the pyroclastic deposit of Sel. 3. B), MDIS-WAC resampled Ti-rich, Mn-rich, Cr-rich and V-rich pyroxene spectra from Cloutis (2002) and Ni-rich pyroxene spectra from White et al. (1971). Spectra are normalized at 0.56 µm but shifted for clarity. C) MgS, MnS and CaS sulfides spectra after thermal alteration from Herbert et al. (2013). CaS spectrum is scaled for clarity. D) Chloride spectra from RELAB: MgCl (WV-JWH-001/C1WV01), CaCl (JB-JLB-G29-B/BKR1JBG29B) and $FeCl_3$ (LW-EAC-001/CALW01.

570 To enhance the contrast and to better analyse the spectral differences, we then performed a
571 continuum-removing of the four-representative cluster spectra from Lermontov area (Fig.
572 22A). When focusing on the pyroclastic deposit and the outer terrain, the major differences
573 between them are observed in the wavelength range 0.55-0.75 μm. The outer terrain minimum
574 peak is located at 0.69 μm while the pyroclastic deposit maximum absorption is shifted towards
575 0.75 μm. By looking at Fig. 22B, this difference could be interpreted as a possible difference
576 in mineralogy with a pyroclastic deposit composition linked with Ni- and Ti-rich pyroxene,
577 while the outer terrain might be dominated by Cr-, and possibly, Mn-rich pyroxene. Moreover,
578 the differences between the pyroclastic spectrum and the outer terrain one around 0.55-0.62
579 μm could be linked with both the presence/absence of MnS and MgS. Indeed, as from Fig.
580 22C, these compounds are characterised by bands localised in this spectral region, as also Mn-
581 rich pyroxene (Fig. 22B) and $FeCl_3$ (Fig. 22D). Although MgCl and CaCl (Fig. 22D) are not
582 showing features in this spectral region, they are suggested as possible hermean volcanic gases
583 too (Zolotov, 2011), therefore, we cannot exclude their presence.
584 Instead, if we compare the field hollows to the pyroclastic and the outer terrain spectra, beyond
585 the difference in slope that is clearly visible in Fig. 21, there is a general difference between
586 the continuum-removed spectra of Fig. 22A. Indeed, the field hollows seem to be
587 systematically less intense in the wavelength range 0.48 - 0.82 μm and the absorption band at
588 0.55 μm is completely absent. This same absence is observable in the vent hollows spectrum
589 too, although the trend the 0.62 – 0.82 μm range is more similar to the pyroclastic one. The
590 band at 0.55 μm could be related to CaS and the small differences at 0.48 μm and 0.62 μm
591 could be related to other volatiles compounds such as MgS and Fe_3Cl. This supports the
592 interpretation that field hollows are less rich in such volatile elements when compared to the
593 pyroclastic material. Moreover, the maximum absorption peak of hollows spectra is localized
594 at 0.82 μm, as the pyroclastic one: this is possibly linked to the Ti-rich pyroxene presence.

595 The similarity in spectral profile between pyroclastic and vent hollows, coupled with the slope
596 differences showing a redder spectrum for vent hollows and a bluer spectrum for field hollows,
597 confirms that hollows' formation mechanism, and hence their spectroscopic appearance, is not
598 disconnected from the composition of the terrain where they form (Lucchetti et al., 2018).
599

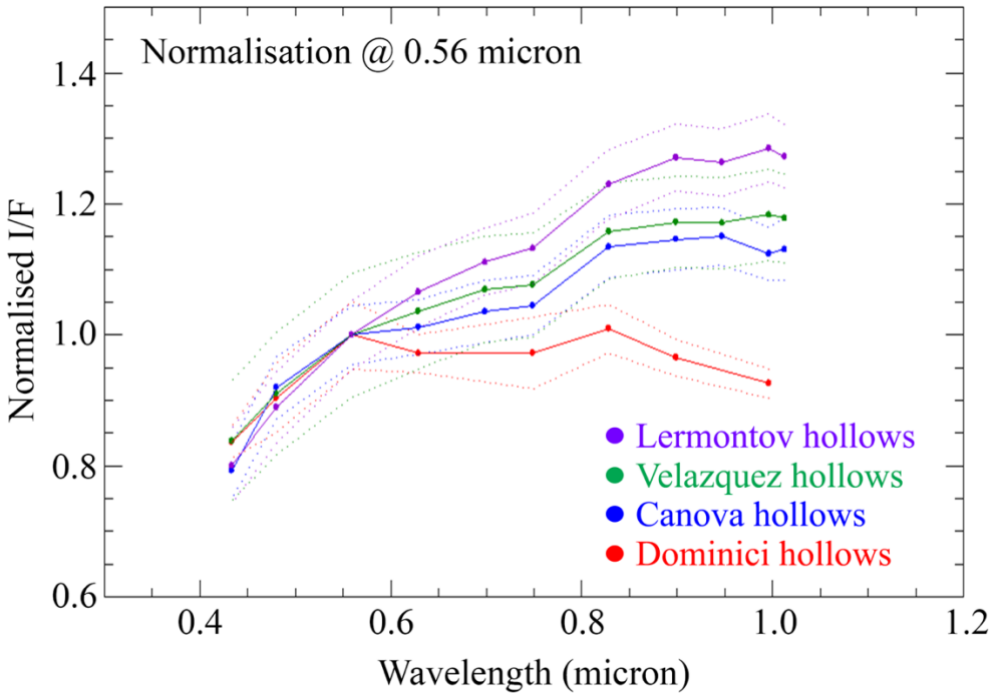

600
601 Fig. 23. Comparison between the spectral behaviour of Lermontov hollows and those analysed in Velazquez,
602 Canova, and Dominici crater (Lucchetti et al., 2018; Vilas et al., 2016).

603 If we finally compare Lermontov hollows spectra to the ones previously obtained on
604 completely different geological settings (Vilas et al., 2016; Lucchetti et al., 2018), we can see
605 that their trend is generally redder/steeper (Fig. 23). This difference is not surprising giving
606 their origin deeply rooted to the pyroclastic activity itself.
607 Velasquez and Lermontov hollows present similar spectra but on Lermontov there is a more
608 pronounced 0.95 μm absorption feature. Among all, the Dominici hollows are the most
609 different ones with two very broad bands in the 0.6-0.8 μm range and above 0.9 μm. Canova
610 hollows, instead, are a sort of transition between the Dominici ones and those of Velasquez and

Lermontov. Moreover, the hollows at Canova crater show a possible shoulder at 0.62 μm and a small absorption at 0.99 μm, not observed on Lermontov.

We recall that these findings must consider the limitation of the MDIS WAC calibration reported in Denevi et al. (2018), hence suggesting caution in interpreting features in MDIS spectra found in individual WAC data sets. Future refinement and improvements to the calibration of the WAC data set will be performed (Denevi et al., 2018) for spectral studies hence improving the use of the individual WAC color sets.

Conclusions

Using both monochromatic MESSENGER MDIS-NAC and multiband MDIS-WAC images we performed a multidisciplinary analysis of the Lermontov crater on Mercury, a 166 km diameter crater where red pyroclastic deposits and bright blue hollows and haloes coexist. We prepared the first high-resolution geological map of the Lermontov floor and its closest surroundings, identifying eight different geologic units and an unnamed bright facula, which covers almost entirely the crater floor in the central and eastern portion.

Moreover, carrying out a statistical analysis of the craters located on Lermontov floor, we derived a modelled retention age ranging between 3.84 and 3.74 $\pm$0.01Ga. Since the thickness of the pyroclastic deposits is not quantitatively known, the derived modelled age can be either the one of the deposits themselves, or the impact age of Lermontov. Previous works described Lermontov as of Mansurian age: our analysis highlights that the crater emplacement is much older, falling in the Late Tolstojan/Calorian timeframe (depending on which time-stratigraphic system is considered).

A detailed analysis of the two pyroclastic deposits of Lermontov returned sizes ranging between 34 and 36 km (the NE one) and 37-41 km (the SW one), comparable to other measured pyroclastic deposit sizes on Mercury. Such deposits are centred on two vents: i) the NE one

636 presents crisp edges, a depth of 0.95 km and when it erupted, its pyroclasts were ejected at a
637 minimum speed of 360 m/s. On the contrary, ii) the Lermontov SW vent has much more
638 degraded edges and it likely erupted with a minimum velocity of 380 m/s. Despite a vent mutual
639 distance of 52 km, the pyroclastic material located in close proximity to both vents has a similar
640 spectrophotometric behaviour. This suggests that the two magmatic chambers that supplied the
641 eruptions might have had a similar chemical composition. An alternative hypothesis is that
642 instead of two volatile reservoirs, there could be a single magmatic chamber that may have
643 alternatively fed both vents, hence resulting in a similar ejected composition.
644 The putative magmatic abundances that could have favoured the Lermontov explosions are
645 comparable to, if not exceeding, the quantity of volatiles detected at terrestrial vents. This
646 supports the interpretation that the hermean crust was not as extremely depleted in volatile
647 material as it was suggested in the past.
648 The pyroclastic deposits located on Lermontov floor have a steep, red spectral behaviour
649 dominated by the presence of a mixture of various pyroxenes containing Ti, Ni and possibly
650 Vanadium. On the contrary, the vents' rims are characterised by several hollows whose spectral
651 slope is bluer that the pyroclastic deposits themselves. By comparing the vent hollows to the
652 field ones located farther out, we observe a 0.62-0.82 μm spectral trend that is more similar to
653 the pyroclastic one. Their band located at 0.55 μm could be related to CaS while the small
654 differences at 0.48 μm and 0.62 μm could be due to the presence of other volatiles compounds,
655 such as MgS and Fe_3Cl. Similar, but less intense absorptions between vent hollows and
656 pyroclastic deposits suggest that i) hollows' formation mechanism, and hence their
657 spectroscopic appearance, is not disconnected from the composition of the terrain where they
658 form, and that ii) vent hollows are less rich in such volatile elements when compared to the
659 pyroclastic deposits.
660

Overall, Lermontov hollows are characterised by steeper spectra with respect to the ones located on completely different hermean geological settings. This means that they entirely formed within the red pyroclastic material, they are shallower than its thickness and they postdate its formation.

We finally underline that the pyroclastic deposits of Lermontov, as well as its vent and field hollows, represent important sources of information about the past and present Mercury planetary structure, composition, volatile content and stress state. They will therefore be target of interest for the future SIMBIO-SYS instrument suite (Cremonese et al., 2020) onboard the ESA-BepiColombo spacecraft.

Acknowledgments:

This research has been realized under the BepiColombo ASI-INAF contract no 2017- 47-H.0. This manuscript is part of a project that has received funding from the European Union's Horizon 2020 research and innovation programme under grant agreement Nº776276 (PLANMAP). The NASA PDS Cartography and Imaging Science Node, as well as the USGS Astrogeology Science Center PILOT Node are acknowledged for providing access to the MDIS dataset used in this work. This research utilizes spectra downloaded by NASA RELAB facility at Brown University.

Data Availability:

The data used in this manuscript can be found at the NASA PDS Cartography and Imaging Science Node, as well as at the USGS Astrogeology Science Center PILOT Node.

686 ----------

687 ## Supplementary Material:

688 The basemaps we used to prepare the geologic map of Lermontov crater and to identify all
689 craters ≥ 0.3 km located inside the crater's floor are indicated in SM Table 1.

690

Basemap	Scale (m/pixel)	Source
MDIS Global monochrome Basemap Data Record BDR (v1)	166	https://astrogeology.usgs.gov/
MDIS Basemap Data Record BDR (v2) (H06)	166	https://pdsimage2.wr.usgs.gov/Missions/MESSENGER/
MDIS Basemap Low-incidence angle - LOI Global Mosaic	166	https://astrogeology.usgs.gov/
MDIS High-incidence angle East - HIE (v2) (H06)	166	https://pdsimage2.wr.usgs.gov/Missions/MESSENGER/
MDIS Basemap Enhanced Color Global Mosaic (*)	665	https://astrogeology.usgs.gov/
MDIS Basemap MD3-Color Global Mosaic (*)	665	https://astrogeology.usgs.gov/
For topography: MESSENGER Global DEM (v2)	665	https://astrogeology.usgs.gov/
For high-resolution topography: Lermontov localized DTM	155	Fassett (2016)

691

692 Supplementary Material Table 1. All basemaps used for the geologic mapping and crater counting are indicated,
693 together with the spatial scale and the source. "*" denotes the basemaps that have been pan-sharpened, as indicated
694 in the main text.

695

The nine mosaic we prepared processing MDIS NAC single frames using the U.S. Geological Survey (USGS) ISIS3 software are indicated in SM Table 2.

Mosaic no.	Scale (m/pixel)	MDIS-NAC used
1	26	DUE TO COVID-19
		I DO NOT HAVE
2	27	ACCESS TO MY OFFICE
		LAPTOP
3	30	
		I WILL INSERT ALL
4	28	NAMES WHEN I WILL
		BE BACK TO THE
5	31	OFFICE
6	37	EN0258717902M.IMG
		EN0258717921M.IMG
		EN0258717941M.IMG
		DUE TO COVID-19
7	48	I DO NOT HAVE
		ACCESS TO MY OFFICE
8	48	LAPTOP
9	48	

		I WILL INSERT ALL
		NAMES WHEN I WILL
		BE BACK TO THE
		OFFICE

699

700 Supplementary Material Table 2. Mosaic number, spatial scale (in m), and list of all the MDIS-NAC images used

701 for the generation of each mosaic.

702

Central wavelength (μm)	**Bandwidth (μm)**	**Peak transmission**
0.433	0.018	0.694
0.480	0.009	0.875
0.559	0.005	0.810
0.629	0.004	0.898
0.699	0.004	0.892
0.749	0.005	0.896
0.828	0.004	0.921
0.899	0.004	0.898
0.947	0.005	0.942
0.996	0.012	0.952
1.013	0.020	0.964

703

704 Supplementary Material Table 3. Central wavelength, bandwidth and peak transmission for all MDIS-WAC filters

705 used in our analysis (Hawkins et al., 2007)

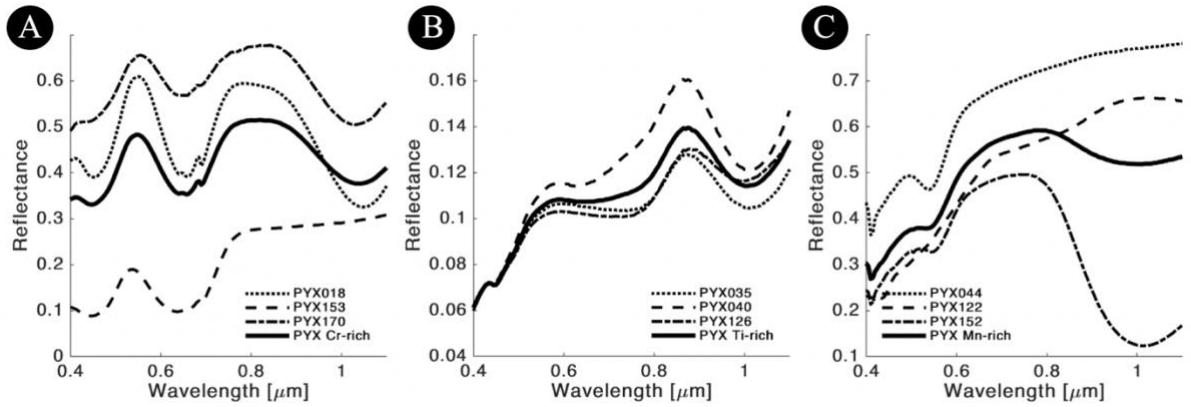

SM Figure 2. Multiple pyroxenes from Cloutis (2002). The solid, thick lines in A, B and C are the average spectra evaluated from the metal-rich sample of the same set.

References:

Asphaug, E., Reufer, A., 2014. Mercury and other iron-rich planetary bodies as relics of inefficient accretion. Nature Geosci 7, 564–568.

Becker, K. J., et al. 2016. First global digital elevation model of Mercury. Paper presented at the 47th Lunar and Planetary Science Conference, Lunar and Planetary Institute, Houston, TX, Astract no. 2959.

Benz, W., et al., 1988. Collisional stripping of Mercury's mantle. Icarus 74, 516–528.

Benz, W., et al., 2007. The origin of Mercury. Space Sci. Rev. 132, 189–202.

Blewett, D.T., et al., 2009. Multispectral images of Mercury from the first MESSENGER flyby: analysis of global and regional color trends. Earth Planet. Sci. Lett. 285, 263–271.

Blewett, D. T., et al., 2013. Mercury's hollows: Constraints on formation and composition from analysis of geological setting and spectral reflectance, J. Geophys. Res. Planets, 118, doi:10.1029/2012JE004174.

Blewett, D. T., et al., 2011. Hollows on Mercury: MESSENGER evidence for geologically recent volatile-related activity. Science, 333 (6051), 1856–1859. https://doi.org/10.1126/science.1211681

Blewett, D. T., et al. 2016. Analysis of MESSENGER high-resolution images of Mercury's hollows and implications for hollow formation. Journal of Geophysical Research: Planets, 121, 1798–1813.

Boynton, W.V., et al., 2007. MESSENGER and the chemistry of Mercury's surface. Space Sci. Rev. 131, 85–104.

Calinski, T., Harabasz, J., 1974. A dendrite method for cluster analysis. Communications in Statistics, 3, 1–27.

Cloutis, E.A., 2002. Pyroxene reflectance spectra: minor absorption bands and effects of elemental sustitutions. Journal of Geophysical Research, 107, E6, 5039, 10.1029/2001JE001590.

Cremonese, G., et al., 2020. *Space Sci. Rev.* (submitted, in revision).

Curtis, C.D., 1964. Applications of the crystal-field theory to the inclusion of trace transition elements in minerals during magmatic differentiation. Geochimica et Cosmochimica Acta, 28, 3, 389-403.

Dalle Ore, C., et al., 2012. Infrared spectroscopic characterization of the low-albedo materials on Iapetus. Icarus 221 (2), 735.

Dalle Ore, C.M., et al. (2018). Ices on Charon: Distribution of H_2O and NH_3 from New Horizons LEISA observations. Icarus 300, 21.

DeHon, R. A., et al., 1981. Geologic map of the Kuiper (H6) quadrangle of Mercury, U.S. Geol. Surv. Misc. Invest. Ser. Map, I-1233.

Denevi, B. W., et al., 2018. Calibration, projection, and final image products of MESSENGER's Mercury Dual Imaging System. Space Science Reviews, 214 (2).

Domingue, D. L., et al. 2015. Mercury's global color mosaic: An update from MESSENGER's orbital observations. Icarus, 257, 477–488. https://doi.org/10.1016/j.icarus.2014.11.027

Du, Q., et al., 2007. On the performance evaluation of pan-sharpening techniques. IEEE Geoscience and Remote Sensing Letters, 4(4), 518-522.

Dzurisin, D., 1977. Mercurian bright patches: Evidence for physio-chemical alteration of surface material? Geophys. Res. Lett., 4(10), 383– 386.

775 Fasset, C.I., 2016. Ames stereo pipeline-derived digital terrain models of Mercury from
776 MESSENGER stereo imaging. Planet. Space Sci. 134, 19-28.
777
778 Fegley, B., Cameron, A.G.W., 1987. A vaporization model for Fe/Si fractionation in the
779 Mercury protoplanet. Earth Planet. Sci. Lett. 82, 207–222.
780
781 Fonti, S., Marzo, G.A., 2010. Mapping the methane on Mars. Astron. Astrophys. 512 (A51), 6
782 pp.
783
784 Gaddis, L.R., et al., 2003. Compositional analyses of lunar pyroclastic deposits. Icarus 161,
785 262–280.
786
787 Galluzzi, V., et al., 2016. Geology of the Victoria quadrangle (H02), Mercury. Journal of Maps
788 12:sup1, 227-238, DOI: 10.1080/17445647.2016.1193777.
789
790 Gerlach, T.M., 1986. Exsolution of H_2O, CO_2, and S during eruptive episodes at Kilauea
791 Volcano, Hawaii. J. Geophys. Res. 91, 12177–12185.
792
793 Goudge, T. A., et al. (2014), Global inventory and characterization of pyroclastic deposits on
794 Mercury: New insights into pyroclastic activity from MESSENGER orbital data, J. Geophys.
795 Res. Planets, 119, 635–658, doi:10.1002/2013JE004480.
796
797 Head, J.W., Wilson, L., 1979. Alphonsus-type dark-halo craters: morphology, morphometry
798 and eruption conditions. Proc. Lunar Planet. Sci. Conf. 10, 2861–2897.
799

800 Head, J. W., et al., 2002. Dark ring in southwestern Orientale basin: Origin as a single
801 pyroclastic eruption, J. Geophys. Res., 107 (E1), 5001, doi:10.1029/2000JE001438.
802
803 Helbert, J., et al., 2013. Visible and near-infrared reflectance spectra of thermally processed
804 synthetic sulfides as a potential analog for the hollow forming materials on Mercury. Earth and
805 Planetary Science Letters, 369-370, 233–238.
806
807 Izenberg, N. R., et al., 2014. The low-iron, reduced surface of Mercury as seen in spectral
808 reflectance by MESSENGER. Icarus, 228, 364–374.
809
810 Kerber, L., et al., 2009. Explosive volcanic eruptions on Mercury: eruption conditions, magma
811 volatile content, and implications for interior volatile abundances. Earth Planet. Sci. Lett. 285,
812 263–271.
813
814 Kerber, L., et al., 2011. The global distribution of pyroclastic deposits on Mercury: The view
815 from MESSENGER flybys 1-3, Planet. Space Sci., 59, 1895–1909.
816
817 Hawkins, S. E., et al., 2007. The Mercury Dual Imaging System on the MESSENGER
818 spacecraft. Space Science Reviews, 131(1–4), 247–338.
819
820 Le Feuvre, M., Wieczorek, M.A., 2011. Nonuniform cratering of the Moon and a revised crater
821 chronology of the inner Solar System. Icarus, 214, 1-20.
822

Lucchetti, A., et al., 2018. Mercury hollows as remnants of original bedrock materials and devolatilization processes: a spectral clustering and geomorphological analysis. Journal of Geophysical Research: Planets. 123. https://doi.org/10.1029/2018JE005722

Lucchitta, B.K., Schmitt, H.H., 1974. Orange material in the Sulpicius Gallus Formation at the southwestern edge of Mare Serenitatis. Proc. Lunar. Sci. Conf. 5, 223–234.

Marchi, S., et al., 2009. A new chronology for the Moon and Mercury. The Astronomical Journal, 137:4936-4948.

Marzo, G. A., et al., 2006. Cluster analysis of planetary remote sensing spectral data. Journal of Geophysical Research, 111, E03002. https://doi.org/10.1029/2005JE002532

Marzo, G. A., et al., 2008. Statistical exploration and volume reduction of planetary remote sensing spectral data. Journal of Geophysical Research, 113, E12009. https://doi.org/10.1029/2008JE003219

Marzo, G. A., et al., 2009. Automated classification of visible and infrared spectra using cluster analysis. Journal of Geophysical Research, 114, E08001. https://doi.org/10.1029/2008JE003250

Michael, G.G., Neukum, G., 2010. Planetary surface dating from crater size frequency distribution measurements: Partial resurfacing events and statistical age uncertainty. Earth Planet. Sci. Lett. 294, 223–229.

Michael, G.G., 2012. Planetary surface dating from crater size–frequency distribution measurements: Spatial randomness and clustering. Icarus, 218, 169-177.

Neukum, G., 1983. Meteoritenbombardement und Datierung planetarer Oberflchen. Habilitation Dissertation for Faculty Membership. University of Munich, p. 186.

Neukum, G., et al., 2001. Cratering records in the inner solar system in relation to the lunar reference system. Space Science Reviews, 96, 55-86.

Pajola, M., et al., 2016a. The Simud–Tiu Valles hydrologic system: a multidisciplinary study of a possible site for future Mars on-site exploration. Icarus 268, 355–381.

Pajola, M., et al., 2016b. Eridania Basin: an ancient paleolake floor as the next landing site for the Mars 2020 rover. Icarus 275, 163–182.

Pajola, M., et al., 2018. Phobos MRO/CRISM visible and near-infrared (0.5-2.5 micron) spectral modeling. Planetary and Space Science, 154, 63-71.

Parente, C., Pepe, M., 2017. Influence of the weights in IHS and Brovey methods for pan-sharpening WorldView-3 satellite images. International Journal of Engineering & Technology, 6(3), 71-77.

Pinilla-Alonso, N., et al., 2011. Iapetus surface variability revealed from statistical clustering of a VIMS mosaic: the distribution of CO2. Icarus 215 (1), 75.

Rava, B., and B. Hapke, 1987. An analysis of the Mariner 10 color ratio map of Mercury, Icarus, 71, 397– 429.

Robinson, M.S., et al., 2008. Reflectance and color variations on Mercury: regolith processes and compositional heterogeneity. Science 321, 66–69.

Schultz, P. H., 1977. Endogenic modification of impact craters on Mercury, Phys. Earth Planet. Inter., 15, 202–219.

Solomon, S. C., et al., 2007. MESSENGER mission overview. Space Science Reviews, 131(1–4), 3–39. https://doi.org/10.1007/s11214-007-9247-6

Spudis, P. D., Guest, J.E., 1988. Stratigraphy and geologic history of Mercury, in Mercury, edited by F. Vilas, C. R. Chapman, and M. S. Matthews, pp. 118–164, University of Arizona Press, Tuscon, Ariz.

Strom, R.G., et al., 1981. Volcanic eruptions on Io. J. Geophys. Res. 86, 8593–8620.

Textor, C., et al. 2003. Emissions from volcanoes. In Emissions of chemical compounds and aerosols in the atmosphere, Claire Granier, Claire Reeves and Paulo Artaxo, Eds., Kluwer, Dordrecht.

Thomas, R. J., et al., 2014. Long-lived explosive volcanism on Mercury. Geophysical Research Letters, 41(17), 6084-6092.

898 Vilas, F., et al., 2016. Mineralogical indicators of Mercury's hollows composition in
899 MESSENGER color observations. Geophysical Research Letters, 43, 1450–1456.
900
901 Wetherill, G.W., 1988. Accumulation of Mercury from planetesimals. In: Vilas, F., Chapman,
902 C.R., Matthews, M.S. (Eds.), Mercury. University of Arizona Press, Tucson, AZ, pp. 670–691.
903
904 White, W. B., et al., 1971. Optical spectra of chromium, nickel, and cobalt-containing
905 pyroxenes. American Mineralogist. Journal of Earth and Planetary Materials, 56(1–2), 72–89.
906
907 Wilson, L., Head, J.W., 1981. Ascent and eruption of basaltic magma on the Earth and Moon.
908 J. Geophys. Res. 86, 2971–3001.
909
910 Wilson, L., Keil, K., 1997. The fate of pyroclasts produced in explosive eruptions on the
911 asteroid 4 Vesta. Meteorit. Planet. Sci. 32, 813–823.
912
913 Wilson, L., 2009. Volcanism in the solar system. Nat. Geosci. 2, 389–397.
914
915 Zolotov, M. Yu., 2011. On the chemistry of mantle and magmatic volatiles on Mercury. Icarus
916 212, 24–41. doi:10.1016/j.icarus.2010.12.014.